



HAL
open science

Non-Fickian dispersion in porous media explained by heterogeneous microscale matrix diffusion

Philippe Gouze, Yasmin Melean, Tanguy Le Borgne, Marco Dentz, Jesus Carrera

► **To cite this version:**

Philippe Gouze, Yasmin Melean, Tanguy Le Borgne, Marco Dentz, Jesus Carrera. Non-Fickian dispersion in porous media explained by heterogeneous microscale matrix diffusion. *Water Resources Research*, 2008, 44, pp.W11416. 10.1029/2007WR006690 . insu-00373705

HAL Id: insu-00373705

<https://insu.hal.science/insu-00373705>

Submitted on 29 Jun 2016

HAL is a multi-disciplinary open access archive for the deposit and dissemination of scientific research documents, whether they are published or not. The documents may come from teaching and research institutions in France or abroad, or from public or private research centers.

L'archive ouverte pluridisciplinaire **HAL**, est destinée au dépôt et à la diffusion de documents scientifiques de niveau recherche, publiés ou non, émanant des établissements d'enseignement et de recherche français ou étrangers, des laboratoires publics ou privés.

Non-Fickian dispersion in porous media explained by heterogeneous microscale matrix diffusion

Philippe Gouze,¹ Yasmin Melean,¹ Tanguy Le Borgne,¹ Marco Dentz,² and Jesus Carrera³

Received 21 November 2007; revised 7 May 2008; accepted 28 July 2008; published 13 November 2008.

[1] Mobile-immobile mass transfer is widely used to model non-Fickian dispersion in porous media. Nevertheless, the memory function, implemented in the sink/source term of the transport equation to characterize diffusion in the matrix (i.e., the immobile domain), is rarely measured directly. Therefore, the question can be posed as to whether the memory function is just a practical way of increasing the degrees of freedom for fitting tracer test breakthrough curves or whether it actually models the physics of tracer transport. In this paper we first present a technique to measure the memory function of aquifer samples and then compare the results with the memory function fitted from a set of field-scale tracer tests performed in the same aquifer. The memory function is computed by solving the matrix diffusion equation using a random walk approach. The properties that control diffusion (i.e., mobile-immobile interface and immobile domain cluster shapes, porosity, and tortuosity) are investigated by X-ray microtomography. Once the geometry of the matrix clusters is measured, the shape of the memory function is controlled by the value of the porosity at the percolation threshold and of the tortuosity of the diffusion path. These parameters can be evaluated from microtomographic images. The computed memory function compares well with the memory function deduced from the field-scale tracer tests. We conclude that for the reservoir rock studied here, the atypical non-Fickian dispersion measured from the tracer test is well explained by microscale diffusion processes in the immobile domain. A diffusion-controlled mobile-immobile mass transfer model therefore appears to be valid for this specific case.

Citation: Gouze, P., Y. Melean, T. Le Borgne, M. Dentz, and J. Carrera (2008), Non-Fickian dispersion in porous media explained by heterogeneous microscale matrix diffusion, *Water Resour. Res.*, 44, W11416, doi:10.1029/2007WR006690.

1. Introduction

[2] Many tracer tests conducted in natural or reconstructed porous media, even in those thought to be macroscopically homogeneous, produce strongly asymmetric breakthrough curves (BTCs) with long recovery times. Often, the late-time part of the BTC (i.e., after the main concentration peak has been recovered) appears to decrease more or less as a power law of time $C(t) \sim t^{-\alpha}$ [Silliman and Simpson, 1987; Adams and Gelhar, 1992; Berkowitz *et al.*, 2000; Meigs and Beauheim, 2001; Becker and Shapiro, 2003; Levy and Berkowitz, 2003; Gouze *et al.*, 2008]. These observations were originally attributed to matrix diffusion. Existing matrix diffusion models led to a value of 1.5 for α [Heer and Haderman, 1994]. However, when BTC tails are observed over a sufficient range of concentrations, α typically ranges between 1.5 and 2.5. The classical Fickian model fails to predict this type of dispersion behavior. In general, strongly asymmetric BTCs will induce apparent scale-dependent values of tracer mean residence time if the

model does not account for the processes that control the BTC tails [Guimerà and Carrera, 2000].

[3] Matrix diffusion is widely cited as a critical transport process controlling the late-time behavior of BTCs [e.g., Shapiro, 2001; Zhou *et al.*, 2007, and references therein]. Indeed, as diffusive transport is slow compared to advection, the late-time behavior of the BTCs should be very sensitive to the tracer transfer rate between the fraction of the porous media where fluid is immobile (matrix) and the water-flowing fraction. Obviously, the effect of matrix diffusion increases with the fraction of matrix accessible to diffusion. A first-order approximation for single rate mass transfers (diffusion or sorption) between the flowing fluid and the matrix was first studied by Coats and Smith [1964] and van Genuchten and Wierenga [1976], which led to the double porosity model for transport. The mathematical formulation consists of adding a sink/source term to the conventional advection-dispersion equation (ADE). In this case the sink/source term is proportional to the average concentration difference between the flowing fluid and the matrix. The importance of matrix diffusion was further investigated in relation to various projects for underground nuclear waste disposal in fractured rocks [e.g., Neretnieks, 1980], and further extended to unconsolidated [Wood *et al.*, 1990] and consolidated porous media [Carrera *et al.*, 1990; Haggerty and Gorelick, 1995]. Carrera *et al.* [1998] proposed a formulation of the sink/source term to account for

¹Géosciences, Université de Montpellier 2, CNRS, Montpellier, France.

²Department of Geotechnical Engineering and Geosciences, Technical University of Catalonia, Barcelona, Spain.

³Institute of Earth Sciences Jaume Almera, CSIC, Barcelona, Spain.

multiple rates (or multirate) mass transfers. These multiple rates emerge from both the transient nature of diffusion in the immobile water zones and the heterogeneity of the matrix [e.g., *Haggerty et al.*, 2000, 2001, 2004]. This class of model is often referred to as a mobile/immobile (MIM) mass transfer model.

[4] The objective of the MIM model is to account for mass exchanges between the moving fluid and zones where the fluid is assumed to be immobile. Following this approach, the system is assumed to be mathematically bimodal, which may appear at first glance to be a critical approximation. Nevertheless, as will be shown in this paper, porous media structures may display this sort of structural bimodality, supporting the intuitively attractive assumption that the mobile domain is advection-dominant, whereas the immobile domain is diffusion-dominant. This approach provides a way to account for the small-scale diffusivity heterogeneity of the rock matrix, which represents typically more than 50% of the media, but is generally not measured. In summary, the MIM model assumes that solutes may be trapped in immobile zones from which they are slowly released by diffusion [*Haggerty and Gorelick*, 1995; *Carrera et al.*, 1998; *Haggerty et al.*, 2000]. The immobile domain includes both dead ends where flow is negligible and intergrain porosity (including trapped pores) where permeability is very low compared to the main permeable structure of the rock [*Haggerty and Gorelick*, 1995]. The contribution of the immobile domain to the change in mobile concentration is modeled by linear mass exchange processes which end up as a source term in the ADE. This source term can be expressed as the convolution product of a time-dependent function, called the memory function, and the time variation of the mobile concentration [*Carrera et al.*, 1998; *Haggerty et al.*, 2000]. The advantages of this formulation are that (1) the memory function depends on the properties of the immobile domain only and is therefore an intrinsic characteristic of the medium, and (2) convolution products are easy to compute, either by Laplace transform of the transport equation or by expansion of the memory function as a sum of exponentials. Alternatively, large residence times may be represented in the framework of continuous time random walks [*Berkowitz et al.*, 2002] in which contaminant (or tracer) particles within the velocity field are represented by random walks in space and time. For instance, a power law distribution of transition times may be used to model power law tailed breakthrough curves. In this case, CTRW formulation is mathematically equivalent to the MIM approach [*Dentz and Berkowitz*, 2003; *Schumer et al.*, 2003].

[5] As highlighted above, the memory function is an intrinsic characteristic of the reservoir rock. To progress toward predictive modeling, this function must be measured on rock samples in manner similar to what is routinely done for other properties such as permeability. *Sardini et al.* [2003, 2007] characterized matrix diffusion from normalized tracer recovery curves from out-diffusion experiments on small samples of microcrystalline granites displaying low porosity (<0.5%). Such recovery curves are proportional to the memory function. Yet, with the exception of studies by *Sardini et al.* [2003, 2007], the memory function is usually estimated from a simplified model assuming a selected density distribution of diffusion rates, allowing

the production of different types of power law tailed BTCs [*Haggerty et al.*, 2000; *Dentz and Berkowitz*, 2003]. Usually, these models consider not only that matrix blocks have simple geometry (e.g., spheres) but also that these blocks are homogeneous in terms of porosity and tortuosity. However, most observations and measurements confirm that matrix blocks are heterogeneous and display nonuniform shapes. Moreover, these models lead to late time power laws with α values of 1.5, while exponents are often larger.

[6] In this paper we first present a noninvasive method for measuring the memory function from diffusion transport calculations using a microscale (i.e., micrometer-scale) description of the matrix structure, whose properties are investigated by X-ray microtomography (XMT). Using this tool, we investigate whether microscale diffusion processes in the reservoir matrix can explain the strongly tailed BTCs measured from macroscale (i.e., meter-scale) tracer experiments. Specifically, we use an example to verify that the mobile-immobile model [*Carrera et al.*, 1998; *Haggerty et al.*, 2000] stipulating that diffusion processes in the immobile domain, at scales smaller than the homogenization scale for which Darcy's law is valid, control the large-scale dispersion measured by in situ tracer tests. For this, we compare the memory functions obtained from diffusion calculations at pore scale to those inferred from tracer tests performed in the same reservoir where the samples came from.

[7] The paper is organized as follow. First, in section 2, we briefly present the reservoir properties and tracer test data. Then, in section 3, the conceptual and mathematical principles used to model dispersion in the framework of the MIM model are reviewed, emphasizing the properties of the memory function in the case of heterogeneous structures. Data analysis and methodology for computing the memory function from XMT images are presented in detail in section 4. Section 5 compares the tracer test BTCs and the memory function obtained from XMT image processing. Our conclusions are presented in section 6.

2. Reservoir Properties and Tracer Test Data

[8] The tracer tests discussed in this paper were performed in a Miocene reef formation situated 50 km from Palma de Mallorca (Balearic Islands). The characteristics of the medium, the tracer test equipment and protocols and the results obtained for the 10 tests performed in well MC2 at depth 94 m are detailed by *Gouze et al.* [2008]. Here we will briefly present the main features concerning the reservoir properties and tracer test data.

[9] The reservoir rock is a pure bioclastic carbonate (calcite) displaying high porosity. Macroscopically observable porosity variations typically occur over vertical distances of five to ten meters and over horizontal distances of ten to a hundred meters. Tracer tests discussed in this paper concern distances smaller than 10 m (i.e., reservoir volumes ranging from 1 to 40 m³). The porosity of the reef distal slope was measured on several samples of distinctly different volumes. The total porosity is 0.35 ± 0.05 whereas the effective porosity (porosity of the permeable cluster) is 0.285 ± 0.015 .

[10] Permeability, measured by pumping tests using the same configuration as for the tracer tests (see below),

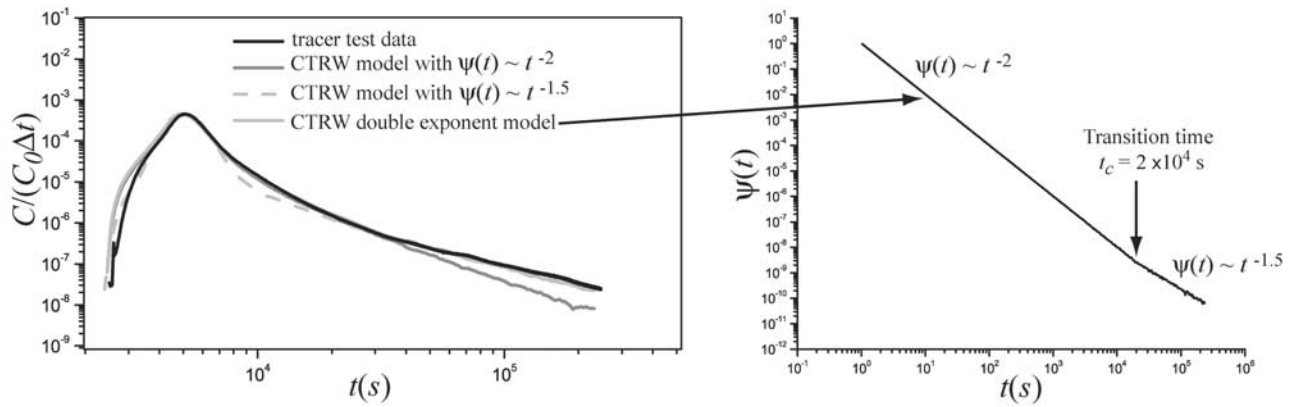


Figure 1. (left) Example of breakthrough curve (BTC) obtained from SWIW tracing experiment at depth 94 m in well MC2 (Ses Sitjoles test site) and CTRW model fitted curves. Concentration, C , is normalized by dividing it by C_0 , the concentration of the injected tracer, and the injection duration, Δt . The unusual shape of the curve tail is modeled by a MIM mass transfer model using the CTRW approach with a dual-slope transition time distribution [Le Borgne and Gouze, 2008]. (right) Dual slope transition time distribution used in the CTRW computations to account for the retention time probability of the tracer in the immobile domain.

is $1.95 \pm 1.10 \times 10^{-12} \text{ m}^2$, whereas measurements on borehole cores (diameter 90 mm) and plugs (25 mm diameter) is $1.35 \pm 1.15 \times 10^{-13} \text{ m}^2$. Meter-scale permeability is therefore apparently 1 order of magnitude higher than centimeter-scale permeability. Nevertheless, it is important to note that centimeter-scale samples are usually chosen (for obvious experimental issues) with no visible centimeter-scale pore, so that it contains fewer large pores than the average in the aquifer.

[11] The tracer tests discussed in this paper are single well injection withdrawal (SWIW) tracer tests. SWIW tracing tests consist in injecting a given mass of tracer in the medium, flushing it radially at constant flow rate using previously pumped reservoir water, and reversing flow after a certain time in order to measure the tracer breakthrough curve at the injection point [Gelhar and Collins, 1971; Tsang, 1995; Haggerty et al., 2001; Khrapitchev and Callaghan, 2003]. This technique presents several advantages. First, the reversal of flow leads to an optimal tracer mass recovery. Second, SWIW tracer tests measure the irreversible dispersion (or mixing) whereas reversible dispersion, that is the spreading due to a long-range correlated path present during the tracer push phase, is canceled during the withdrawal phase [Becker and Shapiro, 2003; Khrapitchev and Callaghan, 2003]. The quantification of the reversible and irreversible dispersion refers to a given scale of observation which, in our case, is the maximal distance moved by the tracer during the SWIW tracer test. More precisely, velocity correlation over a distance smaller than the exploration size will result in irreversible dispersion (diffusion and mixing) whereas spreading due to velocity correlation larger than the exploration size will be canceled [see Gouze et al., 2008, Figure 1]. Thus, the dispersion measured by SWIW tests is caused only by tracer molecules that do not follow the same path on the injection and withdrawal phases. Third, using SWIW tests, tracers can be pushed at different distances from the injection point, thus testing different volumes of the system using a single well. It allows the exploration of the dispersion processes

for increasing reservoir volumes and testing of the predictive nature of the models.

[12] Tracer tests were performed at 94 m depth within the seawater intrusion zone, i.e., more than 20 m below the saline wedge top. In this zone, regional flow is negligible for the tracer test duration under consideration (a few days). Two inflatable packers of 1.5 m long are used to delimit a test zone of 0.675 m long. The tracer is a solution of 20 ppm mass of 99% pure uranine (fluorescent dye) diluted in the formation water previously extracted from the borehole. The geometry of the experiment is predominantly radial cylindrical. The volume of rock, explored by the tracer, ranges from 1 to 40 m^3 depending on the injection duration.

[13] All BTCs display non-Fickian behavior with similar concentration decreases for times longer than the characteristic advection time (t_{ad}). However, BTCs do not display the usual single slope power law concentration decrease $C(t) \sim t^{-\alpha}$ corresponding to the conventional MIM mass transfer model proposed by Carrera et al. [1998] and Haggerty et al. [2000]. At intermediate times $t_{ad} < t < t_c$, the concentration decreases roughly as $C(t) \sim t^{-2}$. Then, at large times ($t > t_c$) the asymptotic decrease is $C(t) \sim t^{-1.5}$ (Figure 1, left). Analyzing the BTCs for distinctly different injection times, using the CTRW approach, Le Borgne and Gouze [2008] explains this slope change by a dual slope transition time distribution that denotes, in terms of the MIM mass transfer model, a dual control of the retention time probability of the tracer in the immobile domain (Figure 1, right).

[14] Whether these distinctly different characteristic times of retention result from immobile domains of distinctly different diffusivities, distinctly different diffusion path lengths or distinctly different immobile regions sizes is difficult to determine by conventional analysis of the porosity structures. Hence, although fully coherent in terms of predictability and scalability, the physical meaning of the dual retention model proposed by Le Borgne and Gouze [2008] is still unclear. A fundamental question is whether this unconventional behavior is controlled by microscale diffusion heterogeneities alone, or influenced by a change in

properties with scale. In the following, we will test the first part of the above mentioned assumption.

3. Conceptual and Mathematical Bases

[15] This section is a review of the formulation of the mobile-immobile mass transfer model assuming that the immobile domain is homogeneous in terms of diffusivity. This means essentially that porosity and tortuosity of the rock matrix is assumed to be spatially constant. The formulation for the heterogeneous case will be developed in section 4.

3.1. Formulation of the Mobile-Immobile Mass Transfer Model

[16] In classical field and laboratory setups, only the flowing fluid (i.e., fluid belonging to the mobile domain) can be retrieved from well(s), streams or outlets ports for tracer concentration monitoring. We are therefore mainly interested in obtaining the representative elementary volume (REV) [de Marsily, 1986] averaged solute concentration of the mobile domain C_m . The mass balance equation (advection-dispersion equation, ADE) modeling the concentration redistribution $C_m(\mathbf{x}, t)$ of single species in the mobile domain is [Coats and Smith, 1964; Carrera et al., 1998; Haggerty et al., 2001; Schumer et al., 2003]

$$\phi_m \frac{\partial C_m}{\partial t} = L(C_m) - F_{im}, \quad (1)$$

where $\phi_m = V_m/V_{tot}$ is the volume fraction of the mobile domain (with mobile volume V_m and total aquifer volume V_{tot}) and $L(C_m)$ is the hydrodynamic transport operator. In (1), $F_{im}(\mathbf{x}, t)$ is a sink/source term that represents the volumetric mass flux ($\text{ML}^{-3}\text{T}^{-1}$) of solute transferred from the mobile zone to the immobile zone per unit volume of aquifer:

$$F_{im} = \phi_{im} \partial C_{im} / \partial t, \quad (2)$$

where $C_{im}(\mathbf{x}, t)$ is the REV averaged solute concentration of the immobile domain at coordinate \mathbf{x} and $\phi_{im} = V_{im}/V_{tot}$ (with the immobile volume V_{im}) the volume fraction of the immobile domain. With the adequate boundary and initial conditions (see below), equation (1) expresses mass balances in time and space.

[17] The mobile domain corresponds to the portion of the aquifer accessible to flowing water. Transport processes in this zone are assumed to be Darcy's scale advection and Fickian dispersion, and therefore the transport operator is given by [de Marsily, 1986]

$$L(C_m) = \nabla \cdot (\mathbf{D} \nabla C_m) - \mathbf{q} \nabla C_m, \quad (3)$$

where \mathbf{D} is the dispersion tensor and \mathbf{q} the Darcy velocity (or specific discharge); $\mathbf{q} = \phi_m \mathbf{v}$ where \mathbf{v} is the mean pore velocity.

[18] The immobile domain corresponds to portions of the aquifer where flow is negligible compared to flow within the mobile domain. The immobile domain includes the fraction of rock matrix containing connected microporosity or intergrain porosity as well as stagnant and trapped water [Haggerty and Gorelick, 1995]. The porosity of the im-

mobile domain is $\phi'_{im} = V'_{im}/V_{im}$, (where V'_{im} is the immobile liquid volume). Note that for the most general case, ϕ_{im} and ϕ_m are spatially distributed values (e.g., $\phi_{im}(\mathbf{x})$) as is a priori the case for \mathbf{D} and \mathbf{q} . In most published studies, the immobile domain is assumed to include the entire mobile-complementary fraction $(1 - \phi_m)$ with a constant effective diffusion d_{im} . As will be shown in section 4, a more accurate description of the geometric parameters controlling diffusion processes requires evaluation of the spatial distribution of $d_{im}(\mathbf{x}')$ in the microporous fraction including stagnant and trapped water. Consequently, for the purpose of generalization, we define at this point $\phi_{im} = 1 - \phi_m - \phi_s$, where ϕ_s is the fraction of the medium that is inaccessible to both advection and diffusion (see section 4).

3.2. Memory Function

[19] For linear mass transfer processes, such as diffusive mass transfer, the concentration in the immobile domain is a linear functional of the concentration in the mobile domain [e.g., Dentz and Berkowitz, 2003],

$$C_{im}(\mathbf{x}, t) = \int_0^t G(t-t') C_m(\mathbf{x}, t') dt' = G(\mathbf{x}, t) * C_m(\mathbf{x}, t), \quad (4)$$

where $*$ denotes the convolution product and G (T^{-1}) the memory function that contains all the information on the mass transfer process, the geometry and the volume fraction of the immobile domain as well as its accessibility to tracer particles issued from the mobile domain. Thus, the sink/source term F_{im} in equation (1) can be expressed by the convolution product [Carrera et al., 1998; Haggerty et al., 2000]

$$F_{im}(\mathbf{x}, t) = \phi_{im} \frac{\partial C_m(\mathbf{x}, t)}{\partial t} * G(\mathbf{x}, t). \quad (5)$$

[20] The memory function $G(t)$ is related to the probability that a tracer particle entering the immobile zone at $t = 0$ remains in it until time t [Haggerty et al., 2004]. The zeroth moment of the memory function $G(t)$ is equal to

$$\int_0^\infty G(t') dt' = \phi'_{im}, \quad (6)$$

where ϕ'_{im} is the microporosity of the immobile region assumed here to be homogeneous.

3.3. Multirate Diffusive Mass Transfer Into Homogeneous Immobile Regions

[21] In natural rocks, immobile zones exhibit microscale heterogeneities (see section 4.3), which imply a distribution of mass transfer rates λ . In an effective modeling approach, the heterogeneous immobile region is replaced by a superposition of homogeneous immobile regions, each of which is characterized by a mass transfer rate λ . The latter is distributed according to the distribution density $P(\lambda)$; $P(\lambda)d\lambda$ is the probability of (T^{-1}) a tracer particle being in an immobile region characterized by a transfer rate in the interval $[\lambda, \lambda + d\lambda]$. Accordingly, the memory function $G(t)$ for diffusive mass transfer into the heterogeneous immobile

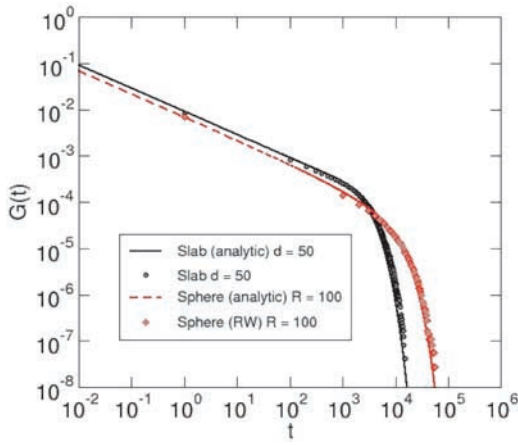


Figure 2. Computed memory function (RW is random walk method) versus analytical solution for a sphere and a slab with identical constant diffusivity.

zone Ω is given by the weighted average over the local memory functions $W(t, \lambda)$, which quantifies mass transfer between the mobile region and the immobile zone characterized by the transfer rate λ [e.g., Haggerty *et al.*, 2000]. This gives

$$G(t) = \int_0^{\infty} P(\lambda) W(t, \lambda) d\lambda. \quad (7)$$

[22] Note that $P(\lambda)$ characterizes both the volumetric distribution of the λ -specific regions in the immobile domain and their accessibility to the tracer particles in the mobile domain. However, there is no evidence that the λ -specific regions have variable access probability. Therefore, it is generally assumed that $P(\lambda)$ is controlled by the volumetric distribution of the λ -specific regions alone.

[23] Diffusive mass transfer into the homogeneous immobile domain Ω_λ is described by the diffusion equation

$$\phi'_{im} \frac{\partial c_{im}(\mathbf{x}', t, \lambda)}{\partial t} = d_{im} \Delta' c_{im}(\mathbf{x}', t, \lambda) \quad (8)$$

with boundary conditions $c_{im}(\mathbf{x}', t, \lambda)|_{\mathbf{x}' \in \partial\Omega_\lambda} = C_m(\mathbf{x}, t)$ at the domain boundary $\partial\Omega_\lambda$ and initial conditions $c_{im}(\mathbf{x}', t=0, \lambda) = 0$, where $c_{im}(\mathbf{x}', t, \lambda)$ is the solute concentration in a unit volume of fluid in the immobile zone and \mathbf{x}' is the position vector in the coordinate system attached to the immobile zone. It is assumed that the length scale of the immobile zone is much smaller than the scale of variation of the mobile concentration so that $C_m(\mathbf{x}, t)$ is constant over the interface between the mobile and immobile regions. The transfer rate is given by $\lambda = d_{im}/l^2$, where l is the characteristic diffusion length and d_{im} the (constant) effective diffusion coefficient in the immobile domain. The average concentration $C_{im}(\mathbf{x}, t, \lambda)$ in the immobile region (per unit volume of immobile region) is given by

$$C_{im}(\mathbf{x}, t, \lambda) = \frac{1}{V_{\Omega_\lambda}} \int_{\Omega_\lambda} c_{im}(\mathbf{x}', t, \lambda) \phi'_{im} d\mathbf{x}', \quad (9)$$

where V_{Ω_λ} is the volume of the (homogeneous) immobile region Ω_λ .

[24] The solution $c_{im}(\mathbf{x}', t, \lambda)$ of (8) can be expressed in terms of the associated Green function $g_{im}(\mathbf{x}', t, \lambda)$ in the following manner:

$$c_{im}(\mathbf{x}', t, \lambda) = \int_0^t g_{im}(\mathbf{x}', t - t', \lambda) C_m(\mathbf{x}', t') dt'. \quad (10)$$

[25] The Green function satisfies (8) for the boundary condition $g_{im}(\mathbf{x}', t - t', \lambda)|_{\mathbf{x}' \in \partial\Omega_\lambda} = \delta(t - t')$. The immobile REV averaged concentration $C_{im}(\mathbf{x}, t)$ is now given by the weighted sum of the average concentrations in the immobile regions. Using (7), (9) and (10), we obtain

$$C_{im}(\mathbf{x}, t) = \int_0^t \left\{ \int_0^{\infty} P(\lambda) \left[\frac{1}{V_{\Omega_\lambda}} \int_{\Omega_\lambda} \phi'_{im} g_{im}(\mathbf{x}', t - t', \lambda) d\mathbf{x}' \right] \cdot C_m(\mathbf{x}, t') d\lambda \right\} dt'. \quad (11)$$

[26] Thus, comparing (11) with (4) and noting that ϕ'_{im} is constant, we identify the memory function with the expression in braces in (11),

$$G(t) = \phi'_{im} \int_0^{\infty} P(\lambda) \left[\frac{1}{V_{\Omega_\lambda}} \int_{\Omega_\lambda} g_{im}(\mathbf{x}', t, \lambda) d\mathbf{x}' \right] d\lambda. \quad (12)$$

Note that the time integral of the Green function is equal to unity and the distribution of transfer rates is normalized. Thus the time integral of the memory over all times is equal to the porosity of the immobile domain (see (6)). By comparing (7) with (12), we identify the local memory function $W(t, \lambda)$ as the expression in square brackets in (12).

[27] Solving (8)–(12), Carrera *et al.* [1998] obtained a solution for the local memory functions $W(t, \lambda)$ for homogeneous spheres, slabs and cylinders. They show that $W(t, \lambda)$ can be expressed as a sum of exponentials of the general form

$$W(t, \lambda) = \lambda \sum_{n=1}^{\infty} a e^{-b_n^2 \lambda t}, \quad (13)$$

where a and b_n are geometrical parameters [see Carrera *et al.*, 1998, Table 1] (e.g., $a = 2/3$ and $b_n = n\pi/3$ for a sphere). Note that (13) holds for the widely used dual-porosity model including the first-order approximation of matrix diffusion. In the latter case, $a = b_n = 1$ for $n = 1$ and $a = b_n = 0$ for $n > 1$; that is, the local memory function is given by $W(t, \lambda) = \lambda e^{-\lambda t}$. Note that single rate diffusive mass transfer into simple homogeneous structures, for which $P(\lambda) = \delta(\lambda - \lambda_0)$ and accordingly $G(t) = W(t, \lambda_0)$ given by (7), can be seen as a multirate first-order mass transfer. For these simple structures, $G(t)$ displays a power law behavior $G(t) \approx A t^{-1/2}$ for times $t \ll \lambda^{-1}$, where $A = \sqrt{\lambda/\pi}$. Figure 2 displays memory functions computed by the random walk algorithm (see section 4.4) for homogeneous slabs and spheres as well as the solutions given by (7), (8) and (13).

[28] Several transfer rate density functions $P(\lambda)$ have been studied by *Haggerty et al.* [2000], including power law, gamma and lognormal distributions. These density functions can be used to model diffusive mass transfer into different immobile structures (distribution of different sphere sizes, mixture of spheres, slabs or any complex structures, etc.). However, these structures are generally unknown a priori.

[29] For weakly variable velocity fields, such as implied by the Fickian advection-dispersion model in the mobile domain, $C_m(t)$ can be approximated by [*Haggerty et al.*, 2000]

$$C_m(x_{obs}, t) \approx -t_{ad} C_0 \Delta t \frac{\partial G(t)}{\partial t}, \quad C_m(\mathbf{x}, t = 0) = 0 \quad (14)$$

for times $t_{ad} \ll t \ll t_{res}$, where t_{res} is the residence time in the immobile regions. In (14), C_0 is the pulse concentration at the inlet boundary, Δt the duration of the pulse and t_{ad} the typical advection time required by the solute to move from the inlet to the observation point $x_{obs}(t_{ad} = x_{obs}/\nu)$. At late times, i.e., when the concentration pulse has moved far past the observation location \mathbf{x}_{obs} ($t \gg t_{ad}$), the concentration in the mobile domain is almost independent of hydrodynamic dispersion: $|\mathbf{D}\nabla C_m| \ll |\nu C_m|$. It is then clear from (14) that the occurrence of a power law tailed BTC ($C_m(t) \sim t^{-(\gamma+1)}$) requires $G(t)$ to scale as $G(t) \sim t^{-\gamma}$. This behavior would persist infinitely if the tracer could assess longer diffusion paths (implying longer residence times) as time increases. This could occur in a true fractal system. However, in natural porous media, a maximum diffusion length, corresponding to the largest spatial structures, is expected, and the power law decrease persists until t_{res} which denotes the maximum residence time in the immobile domain. The value of t_{res} , that corresponds to the time when the mobile concentration decreases faster than $t^{-(\gamma+1)}$, cannot in general be measured in the field as it requires larger acquisition times and higher resolutions than are presently technically feasible. Moreover, the value of t_{res} is difficult to predict from a model because it is controlled by both the largest possible diffusion paths and the probability of a tracer particle visiting recurrently several of these diffusion zones, which depends strongly on the structure of the mobile domain. Implications of such cutoff scales are discussed by *Dentz et al.* [2004] and will not be investigated further here because tracer test BTCs were not recorded up to t_{res} .

4. Measuring the Memory Function of the Mallorca Limestone

[30] Here, we will focus on setting up a direct procedure for calculating the memory function of the Mallorca limestone. Contrary to what was presented above, we first assume that the immobile domain is heterogeneous both in terms of geometry and diffusivity distribution. This procedure is relatively simple: first we use X-ray microscale tomography (XMT) images to characterize the immobile domain properties, and then we solve the diffusion problem in the immobile zones by particle tracking.

[31] In practice, the separation between the mobile and immobile zones is usually made on conceptual macroscopic representations of the medium (e.g., matrix block intersected by fractures) and not on knowledge of the flow rate

distribution. In this paper, we focus on macroscale (or Darcy-scale) homogeneous and microscale highly heterogeneous porous media, with the aim of determining pore-scale distributions and diffusivity properties of the immobile domain.

4.1. Experimental Setup for X-Ray Microtomography

[32] XMT was used to investigate the pore space of Mallorca limestone (borehole MC2, depth 94 m). Data were collected using the BM5 beam line of the European Synchrotron Radiation Facility (Grenoble, France). XMT is a noninvasive visualization technique producing a 3-D map of the X-ray attenuation of the material. For a given energy of the incident X-ray beam (here 40 keV), attenuation depends on the chemical composition of the rock (which relates closely to the atomic number of its components) and on the density (the mass fraction of rock per volume). In monocrystalline rock, such as the sample studied here, XMT images are density distributions of the rock only, or in other words, 3-D porosity maps.

[33] Cylindrical minicores of 10 mm diameter and 18 mm length were sampled from the borehole core at a depth corresponding to the SWIW tracer tests (i.e., 94 m). Each sample was placed on a rotating bench and 1200 X-rays were recorded at increasing angles ranging from 0 and 180 degrees (i.e., one X-ray every 1/6.66 degree). In our procedure, the monochromatic X-ray beam passes through the sample and then reaches the scintillator, which converts the beam to visible light that is recorded by a high-resolution digital 2048×2048 pixels CCD camera. Using a specific inversion algorithm (implementing the Radon transform, see *Stanley* [1983]), X-rays are processed to finally obtain a matrix of 2048^3 values, each representing the integrated porosity (encoded as real 16 bits) on a cube, named a voxel, of side length $5.01 \mu\text{m}$. Subsequently, data are converted to 8-bit integers, such that voxel values increase with increasing density or decreasing porosity. By convention, porosity maps are displayed as gray level images. Voids are black and massive rock is white. Intermediate gray levels are voxels with different densities, attributed to different microporosities.

[34] The occurrence of such microporosity resulting from pores smaller than the resolution of the optical line was confirmed by higher-resolution imaging (for example $1.7 \mu\text{m}$) of subvolumes of the same minicore using the same beam but with a different optical line, and by BEM images [*Gouze et al.*, 2008].

4.2. Analysis of the Microstructures From XMT Images

4.2.1. Macroporosity

[35] The first data processing step consists in identifying the macroporosity. The histogram of the gray level distribution is an overlapping bivariate distribution where the wide peak at higher attenuation coefficient values is associated with voxels containing a fraction of solid phase (hereafter named matrix), while the narrow peak at lower attenuation coefficient values is associated with the void phase. To discriminate each voxel as being either void or rock matrix, we segment the image using a growing-region algorithm [*Noiriel et al.*, 2007]. Raw data and segmented data are presented in Figure 3. The segmented volumes are stored in a matrix of bytes, corresponding to binary values,

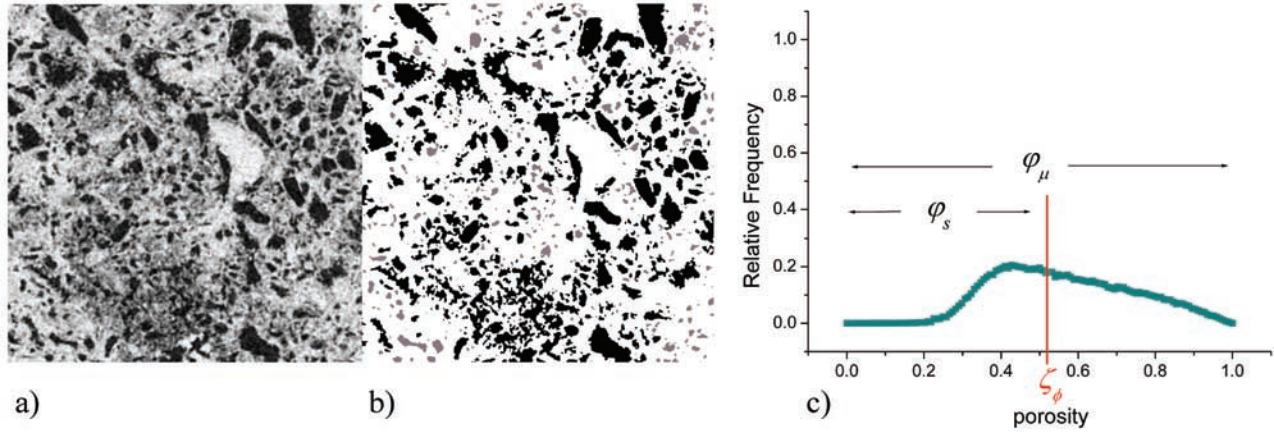


Figure 3. Numerical cross sections in a sample (sample code S94_1_1) of Mallorca limestone cored at 94 m: (a) initial X-ray absorption; (b) ternary image displaying connected porosity (black), rock matrix (white), and unconnected porosity (gray); and (c) histogram of the matrix porosity (symbols as defined in Figure 6).

either 0 (void phase) or 1 (matrix phase). We then obtain the fraction ϕ_{void} of macropores (size from several microns to a few millimeters).

4.2.2. Connected Cluster

[36] The next step consists in determining the percolation clusters, or sample-spanning clusters, which are the networks of pores connected to the boundaries of the sample, and the unconnected pores, using a cluster-labeling algorithm (e.g., *Stauffer and Aharony [1994]*). For our samples, we identified only one single percolation cluster accessible to macroscopic advection across the system. For example, the connected porosity, ϕ_c , is 0.2204, and the unconnected porosity, ϕ_{nc} , is 0.0626 for section S4 (Figure 4). Then, the initial gray level image (renormalized between 2 and 255) is superposed with the segmented image in order to obtain a new image in which label 0 corresponds to connected macroporosity, label 1 to unconnected porosity, and labels ranging from 2 to 255 to the microporous fraction ϕ_μ (called matrix) with inframetric water-filled pores and throats partially interconnected. Label 255 corresponds to massive rock.

4.2.3. Stagnant Water (Dead Ends and Overhangs)

[37] At this stage, the mobile and immobile fraction of the connected macroporosity phase must be evaluated. To do so, we apply a specific algorithm to determine the fraction of the connected macroporosity voxels belonging to the mobile domain for each of the six principal directions in a cubic subsample of the minicore. Then the final nondirectional evaluation of the mobile domain is given by the union of the 6 data sets. For each of the six directions, the procedure requires two steps. First, a simple grass fire algorithm is applied to label each of the voxels (of the connected macroporosity cluster) according to the time progression of the grass fire lighted from one of the six faces of the cube. When all the voxels are labeled, a down gradient search is performed starting from the face opposite the grass fire source. At each of the decremental values of the labeled voxels, neighboring voxels are considered to belong to the mobile phase if their values are equal or lower than the voxel under consideration. The procedure is sketched in Figure 5. As all of the six directions in the

cube are processed and the six mobile regions added, the mobile and immobile fractions of the connected porosity can be identified (Figure 5). The accuracy of this procedure is verified by computing the permeability tensor solving the flow problem (i.e., the Stokes equation with around 10^8 unknowns [*Bernard et al., 2005*]) in the mobile domain meshed using the XMT images taken before and after removing the immobile connected zones. Comparison of the two computed permeability tensors shows a difference of less than 7% on each of the tensor components whereas the mobile porosity is reduced by about 27% by removing the immobile connected zones ϕ_{im} ($\phi_c = 0.274$ and $\phi_m = 0.176$, with $\phi_m = \phi_c - \phi_{im}$, see Figure 6). These calculations demonstrate that the removed part of the macroporosity is

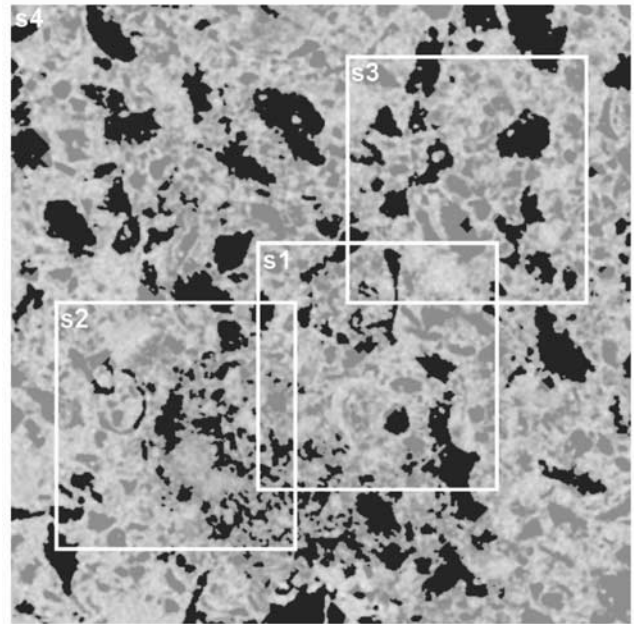


Figure 4. Locations of cross sections S1, S2, and S3 (size 1 mm \times 1 mm) in the cross section S4 (size 2.5 mm \times 2.5 mm).

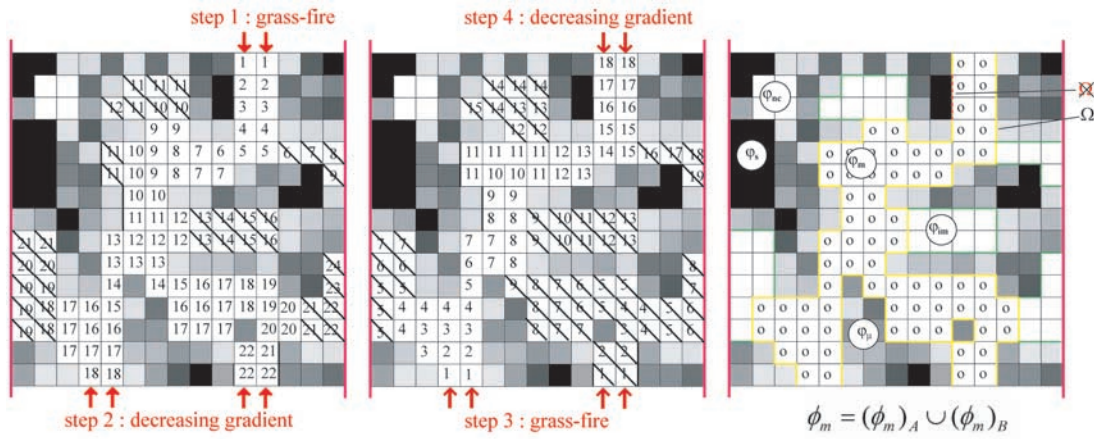


Figure 5. Schematic representation of the algorithm for identifying the stagnant water fraction of the macroporosity. The procedure is displayed here for one direction only (for better visibility) on a 2-D structure. For a 3-D structure, twelve steps are required, i.e., four steps per direction.

not participating to the permeability of the mobile zone, i.e., that the removed pixels belong to the immobile domain.

4.2.4. Effective Porosity for Diffusion in the Immobile Domain

[38] Similar to what is observed for macroporosity, a portion of the microporosity is formed by unconnected voids. However, it is impossible to determine the porosity available for diffusion from analysis of micropore connectivity on the basis of XMT images because the features are smaller than the XMT resolution.

[39] In terms of a continuous model, forming a connected cluster of pores requires porosity above a given threshold. This threshold depends on the pore size distribution and the pore shape anisotropy, as well as the tracer molecule size which in our case is small: $\sim 6.5 \times 10^{-10}$ m. The porosity at the percolation threshold for idealized 2-D media, ζ_ϕ , ranges usually from 0.4 for randomly oriented ellipsoidal pore shape model [Garboczi et al., 1995] to 0.62 and 0.67 for randomly distributed square and disc pore shape model

respectively, while most of the lattice models display values around 0.6 [Balberg, 1985; Torquato, 2001; Baker et al., 2002; Hunt, 2005; Neher et al., 2008]. Values of ζ_ϕ for natural rocks and specifically grainstones (not fractured) are sparse and always indirectly obtained using image processing, for instance. However, it can be deduced from idealized 2-D media, that the expected value for ζ_ϕ is around 0.6 ± 0.05 for cross sections in porous media with weakly anisotropic pores.

[40] On the XMT image, the effective porosity of each voxel belonging to the immobile domain is equal to its porosity if $\phi'_{im} \geq \zeta_\phi$ and null otherwise. The fraction ϕ_s is removed from the immobile domain. Nevertheless, part of the domain where $\phi'_{im} \geq \zeta_\phi$ can be entirely surrounded by solid voxels so that a remaining part of the domain, where $\phi'_{im} \geq \zeta_\phi$, is inaccessible to diffusion. Specific image processing techniques can be used to spot these voxels, but a more efficient way to perform this correction is to deduce them from the computation of the memory function.

V_{tot} / V_{tot}					
φ_{void}				φ_μ	MT segmented data
φ_c		φ_{nc}			
φ_m	φ_{im}			$\zeta_\phi \Rightarrow$	Grass-fire / down gradient
φ_m	φ_{im}				
Mobile domain ϕ_m	Immobile domain $\phi_{im} = V_{im} / V_{tot} = (1 - \phi_m - \varphi_s)$		Solid (no diffusion)	Parameters for the MIM mass transfer model	
$\phi'_{im} = V^l_{im} / V_{im}$			Parameter for the diffusion model		

Figure 6. Parameter summary table. Here ϕ_{im} is the volume fraction of the immobile domain and ϕ'_{im} is the effective porosity of the immobile domain (the porosity available for diffusion in the immobile domain).

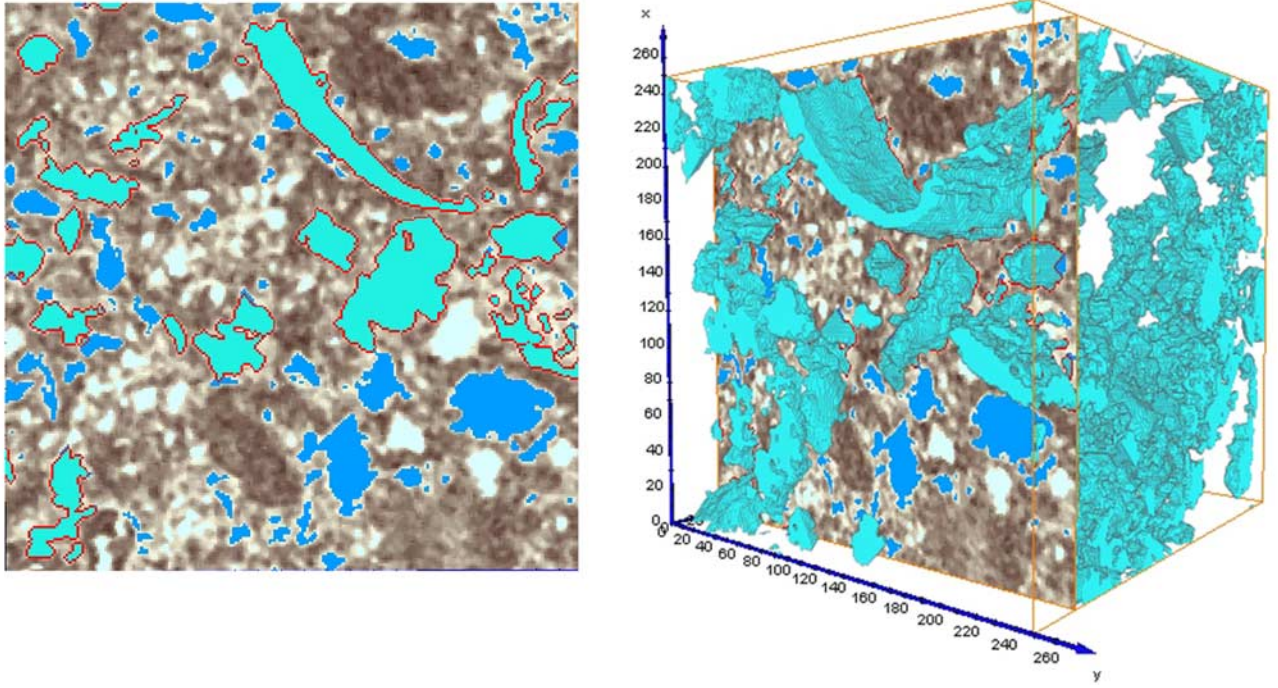


Figure 7. (left) Numerical cross section. (right) Three-dimensional volume rendering representation of a subvolume in sample S94_1_1. The mobile fraction of the connected macroporosity is displayed in cyan, the immobile fraction is displayed in blue, and the porosity of the microporous phase is displayed in shades of gray (dark and light gray denote low and high porosity, respectively). The interface between the mobile domain and the immobile domain is shown by a red line. Coordinates are given in pixels (pixel size $5.01 \mu\text{m}$).

A detailed description of the procedure is given in section 4.5. The control of ζ_ϕ on $G(t)$ will be considered in section 5.1.

4.2.5. Result for Cross Section S4

[41] S4 is a 510 by 510 pixel cross section (see Figure 4). The connected macroporosity fraction ϕ_c is 0.2204, the mobile fraction ϕ_m is 0.1639 and the immobile fraction ϕ_{im} is 0.0565. Now, we reintroduce the original gray level of the rock matrix and label the voxels belonging to the immobile fraction of the macroporosity with the same value as for the unconnected porosity (voxel label = 1). Finally, S_Ω , the interface between the mobile domain and the immobile domain, including ϕ_{im} and ϕ_{nc} , is identified (Figure 7). Adding the unconnected macroporosity fraction, the mobile macroporosity fraction, the immobile macroporosity fraction and the microporosity of the matrix, gives us the total porosity of the medium ϕ_{tot} . The total porosity given by image processing is $\phi_{tot} = 0.3225$. This result obtained on cross sections is in close agreement with the total porosity measured on large size samples (i.e., $40 \times 80 \text{ mm}$) and deduced from standard borehole logging at depth 94 m (i.e., $32 < \phi_{tot} < 36\%$). Note that cores ($18 \times 10 \text{ mm}$) displaying large pores (i.e., centimeter-scale pores) are obviously not selected for XMT; it is therefore not surprising that the computed porosity is close to the lowest value measured on larger size samples and in situ.

4.3. Diffusive Mass Transfer Into a Heterogeneous Immobile Zone

[42] For diffusive mass transfer in geological media such as the Mallorca limestone under consideration, the immobile domain is characterized by a complicated microstruc-

ture that causes the microporosity and tortuosity and thus the diffusion coefficient in the immobile domain to vary spatially i.e., $\phi'_{im} = \phi'_{im}(\mathbf{x}')$, $\tau_{im} = \tau_{im}(\mathbf{x}')$ and $d_{im} = d_{im}(\mathbf{x}')$, respectively. The immobile domain is formed by several immobile clusters. Diffusive mass transfer into a single immobile cluster Ω is described by the diffusion equation

$$\phi'_{im}(\mathbf{x}') \frac{\partial c_{im}(\mathbf{x}', t)}{\partial t} = \nabla' \cdot d_{im}(\mathbf{x}') \nabla' c_{im}(\mathbf{x}', t) \quad (15)$$

with boundary condition $c_{im}(\mathbf{x}', t)|_{\mathbf{x}' \in \partial\Omega} = C_m(\mathbf{x}, t)$ at the domain boundary $\partial\Omega$ and initial condition $c_{im}(\mathbf{x}', t=0) = 0$. The spatially variable diffusion coefficient $d_{im}(\mathbf{x}')$ in the immobile region depends on the microporosity $\phi'_{im}(\mathbf{x}')$ and tortuosity $\tau_{im}(\mathbf{x}')$ according to the relation

$$d_{im}(\mathbf{x}') = d_0 \phi'_{im}(\mathbf{x}') / \tau_{im}(\mathbf{x}'), \quad (16)$$

where d_0 is the molecular diffusion coefficient.

[43] The tortuosity of the diffusion path is a parameter that is very difficult to measure. Tortuosity has no simple or universal definition [Dullien, 1992; Ben Clennell, 1997]. It is a lumped parameter that is used to represent the sinuosity and interconnectedness of the pore space for a given transport process, here diffusion. Often, it is assumed that the inverse of tortuosity scales as a power law of porosity for porosities ranging from 0.4 to 0.5 [Ben Clennell, 1997; Adler and Thovert, 1998; Avellaneda and Torquato, 1991; Dias et al., 2006]. For lower values of porosity, it is probable that porosity alone does not explain tortuosity. Nevertheless, in the absence of better information, this

formulation is a workable approximation and is consistent with the required relationships for the boundary conditions, i.e., $\tau = 1$ when $\phi'_{im} = 1$ (in stagnant and trapped water) whatever the value of exponent n , and $\tau \gg 1$ at the threshold ζ_ϕ for $n > 1$. Therefore, in the following, tortuosity is assumed to be expressed by an inverse power of the immobile porosity, $\tau_{im}(\mathbf{x}') = \phi'_{im}(\mathbf{x}')^{-n}$, and subsequently the diffusion in the immobile domain is given simply by

$$d_{im}(\mathbf{x}') = d_0 \phi'_{im}(\mathbf{x}')^{1+n}. \quad (17)$$

The average concentration in the immobile cluster Ω is given by

$$C_{im}(\mathbf{x}, t) = \frac{1}{V_\Omega} \int_{V_\Omega} \phi'_{im}(\mathbf{x}') c_{im}(\mathbf{x}', t) d\mathbf{x}'. \quad (18)$$

[44] The solution of (15) can be expressed using the Green function $g_{im}(\mathbf{x}', t - t')$, which satisfies (15) for the boundary condition $g_{im}(\mathbf{x}', t - t')|_{\mathbf{x}' \in \partial\Omega} = \delta(t - t')$. The immobile concentration $c_{im}(\mathbf{x}', t)$ can be written as

$$c_{im}(\mathbf{x}', t) = \int_0^t g_{im}(\mathbf{x}', t - t') C_m(\mathbf{x}, t') dt'. \quad (19)$$

[45] The immobile concentration $C_{im}(\mathbf{x}, t)$ is given by the average of $c_{im}(\mathbf{x}', t)$ over the heterogeneous immobile domain. Thus, using (18) and (19), we obtain

$$C_{im}(\mathbf{x}, t) = \int_0^t \left[\frac{1}{V_\Omega} \int_{V_\Omega} g_{im}(\mathbf{x}', t - t') \phi'_{im}(\mathbf{x}') d\mathbf{x}' \right] C_m(\mathbf{x}, t') dt'. \quad (20)$$

[46] By comparing (20) with (4), we identify the memory function with the expression inside the square brackets in (20). Thus, $G(t)$ is given in terms of the spatial average of the Green function $g(\mathbf{x}', t)$ over the immobile domain,

$$G(t) = \frac{1}{V_\Omega} \int_{V_\Omega} g_{im}(\mathbf{x}', t) \phi'_{im}(\mathbf{x}') d\mathbf{x}'. \quad (21)$$

[47] In other words, the memory function $G(t)$ can be obtained from the solution of (15) for an instantaneous unit pulse at the mobile-immobile interface. The time integral over the memory function is equal to the spatially averaged immobile porosity

$$\int_0^\infty G(t) dt = \frac{1}{V_\Omega} \int_{V_\Omega} \phi'_{im}(\mathbf{x}') d\mathbf{x}' \equiv \langle \phi'_{im} \rangle, \quad (22)$$

because the time integral over the Green function is unity.

4.4. Calculating the Memory Function Using XMT Images

[48] In the following, we reformulate the transport problem in terms of a Langevin equation [e.g., Risken, 1996] in order to solve (15) for the Green function $g_{im}(\mathbf{x}', t)$ using

random walk simulations. For this purpose, we define the concentration $g(\mathbf{x}', t)$ per volume of immobile zone,

$$g(\mathbf{x}', t) = g_{im}(\mathbf{x}', t) \phi'_{im}(\mathbf{x}', t). \quad (23)$$

[49] The latter satisfies the transport equation,

$$\frac{\partial g(\mathbf{x}', t)}{\partial t} = \nabla' \cdot d_{im}(\mathbf{x}') \nabla' \frac{g(\mathbf{x}', t)}{\phi'_{im}(\mathbf{x}')}, \quad (24)$$

with the boundary condition $g(\mathbf{x}', t)|_{\mathbf{x}' \in \partial\Omega} = [g_{im}(\mathbf{x}', t) \phi'_{im}(\mathbf{x}')]|_{\mathbf{x}' \in \partial\Omega} = \delta(t) \phi'_{im}(\mathbf{x}')|_{\mathbf{x}' \in \partial\Omega}$. With the above definitions and according to (21), the memory function can be expressed as

$$G(t) = \frac{1}{V_\Omega} \int_{V_\Omega} g(\mathbf{x}', t) d\mathbf{x}'. \quad (25)$$

[50] The diffusion equation (24) for the Green function $g(\mathbf{x}', t)$ is solved by random walk simulations based on the equivalent Langevin equation. First however, we rescale time in (24) according to $t = \tau_d t'$, where τ_d is a typical diffusion timescale (see below). This yields

$$\frac{\partial g_\tau(\mathbf{x}', t')}{\partial t'} = \tau_d \nabla' \cdot d_{im}(\mathbf{x}') \nabla' \frac{g_\tau(\mathbf{x}', t')}{\phi'_{im}(\mathbf{x}')}, \quad (26)$$

where we now specify the boundary condition $g_\tau(\mathbf{x}', t')|_{\mathbf{x}' \in \partial\Omega} = C_0 \delta(t')$. As can be shown by a simple scaling argument, the Green function $g(\mathbf{x}', t)$ is related to $g_\tau(\mathbf{x}', t')$ by

$$g(\mathbf{x}', t) = \frac{g_\tau(\mathbf{x}', t/\tau_d)}{\tau_d C_0}. \quad (27)$$

[51] This can be checked by inspection. The Langevin equation equivalent to the diffusion equation (26) can be expressed in the Ito discretization as [e.g., Risken, 1996]

$$\frac{d\mathbf{x}'(t')}{dt'} = \frac{\nabla' d_{im}(\mathbf{x}'(t'))}{\phi'_{im}(\mathbf{x}')} + \sqrt{2\tau_d \frac{d_{im}(\mathbf{x}'(t'))}{\phi'_{im}(\mathbf{x}')}} \xi(t'), \quad (28)$$

where $\xi(t')$ is a delta-correlated white noise. The diffusion coefficient $d_{im}(\mathbf{x}')$ is now given by

$$d_{im}(\mathbf{x}') = \frac{\varepsilon^2}{2\tau_d D} \phi'_{im}(\mathbf{x}')^{2(1+n)}, \quad (29)$$

where D is the dimensionality of space. Comparing (16) and (29), we identify the molecular diffusion coefficient $d_0 = (\varepsilon \phi'_{im})^2 / (2\tau_d D)$. The diffusion-scale τ_d determines the strength of molecular diffusion; $\varepsilon = aL$ is a small number with $0 < a < 1$ and L the length of a voxel.

[52] For the numerical implementation of (28) in a random walk scheme, the above Langevin equation is discretized in nondimensional time as

$$\mathbf{x}'_{N+1} = \mathbf{x}'_N + \frac{\nabla'(\phi'_{im}(\mathbf{x}') \omega(\mathbf{x}'_N))}{\tau_d \phi'_{im}(\mathbf{x}')} \Delta t' + \sqrt{2\omega(\mathbf{x}'_N) \Delta t'} \xi_N, \quad (30)$$

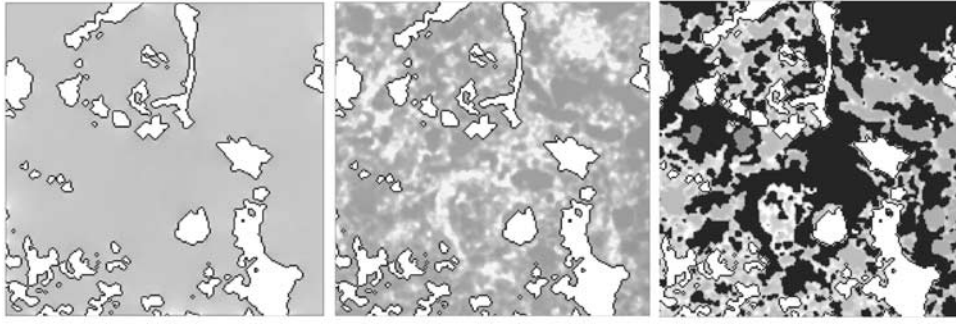


Figure 8. Rate-of-visit map (cross section S1, size 1 mm \times 1 mm) in the immobile domain for $N(0) = 10^9$. (left) Porosity of the immobile zone assumed to be homogeneous $\phi'_{im}(\mathbf{x}') = \langle \phi'_{im}(\mathbf{x}') \rangle$. (middle) Porosity heterogeneity of the immobile domain $\phi'_{im}(\mathbf{x}')$ taken into account with $\zeta_\phi = 0$. (right) Porosity heterogeneity of the immobile domain $\phi'_{im}(\mathbf{x}')$ taken into account with a value of the porosity at the percolation threshold set to $\zeta_\phi = 0.5$. White areas bounded by a black line represent the mobile domain; black areas represent the fraction of rock, ϕ_s , where porosity is lower than the threshold value ($\phi'_{im} < \zeta_\phi$); and gray-scale areas represent the fraction of rock accessible for diffusion ($\phi'_{im} > \zeta_\phi$). Dark gray areas correspond to a low rate of visit, whereas light gray denotes a high rate of visit.

where

$$\omega(\mathbf{x}') = \frac{\varepsilon^2}{2D} \phi'_{im}(\mathbf{x}')^{2n+1}. \quad (31)$$

[53] In the following, we choose the nondimensional time increment $\Delta t' = 1$ and the random space increment $\xi_N = \sqrt{D}r_N$ where r_N are independent random variables that are uniformly distributed over the D -dimensional unit sphere. Thus, ξ_N have zero mean and unit variance and for large N their sum well approximates a Gaussian displacement according to the central limit theorem. Nondimensional time is parameterized by the number of steps of the random walk, $t'_N = N$. During the first step, N_S random walkers (typically $N_S \geq 10^9$) are released, with an initial uniform distribution over the small volume $V_{S\Omega} = \varepsilon S_\Omega$ at the mobile-immobile interface. For $N > 0$, the mobile-immobile interface is an absorbing boundary.

[54] The concrete implementation of the random walk (30) is as follows. At each jump, a random walker can move to any point located at the surface of a sphere of radius $r = \sqrt{2D\omega(\mathbf{x}')$ centered at its initial position. If ϕ'_{im} is space-dependent, i.e., spatially distributed in the immobile domain, a walker can move through several (2 or 3) voxels of distinctly different porosities during $\Delta t'$. In order to determine the exact path length and position at the next step, a recursive procedure is implemented which accounts for the advective correction term $\nabla \cdot d_{im}(\mathbf{x})$ in (24).

[55] At each jump try, there are three possible movements. (1) The particle hits a nonpermeable solid grain; that is, the particle attempts to jump in a voxel of local porosity, ϕ'_{im} , smaller than a given threshold ζ_ϕ . In this case the jump is not performed and a new random position is selected. (2) The move is successful and a new particle position is recorded. (3) The particle jumps outside the immobile domain (i.e., crossing S_Ω). The total number of random walkers inside the immobile domain $N_V(t'_N)$ is recorded as function of time until the last particle leaves the immobile domain.

[56] This numerical random walk scheme implements the initial condition $g_\tau(\mathbf{x}', t'_N = 0) = 0$ and the boundary condition,

$$g_\tau(\mathbf{x}', t'_N) \Big|_{\mathbf{x}' \in \partial\Omega} = C_0 \delta_{N0}, \quad (32)$$

where the distribution density at the boundary is $C_0 = \frac{1}{V_{S\Omega}}$. The total particle density in the immobile zone Ω is given by

$$C_\tau(t'_N) = \frac{1}{V_\Omega} \int_{V_\Omega} d\mathbf{x}' g_\tau(\mathbf{x}', t'_N) = \frac{N_V(t'_N)}{N_S V_\Omega} \quad (33)$$

with V_Ω the volume of the immobile domain. According to (21) and using (27) and (33), we obtain the following expression for the memory function,

$$G(t_N) = \frac{C_\tau(t_N/\tau_d)}{C_0 \tau_d}, \quad (34)$$

with $t_N = t'_N \tau_d = N \tau_d$. Inserting (33) into (34) using $C_0 = 1/V_S = 1/(\varepsilon S_\Omega)$, we obtain

$$G(t_N) = \frac{S_\Omega}{V_\Omega} \frac{\partial N_V(t_N/\tau_d)}{\tau_d N_S} \quad (35)$$

with $\tau_d = \varepsilon^2/(2Dd_0)$. The condition to obtain a pertinent evaluation of the memory function using (35) is $\varepsilon S_\Omega \ll V_\Omega$.

4.5. Correction for Removing the Unconnected Parts of the Mobile Domain

[57] In heterogeneous media, a part of the immobile domain where $\phi'_{im} > \zeta_\phi$ is inaccessible to the tracer diffusion because it is entrapped in the solid part of the matrix (i.e., where $\phi'_{im} < \zeta_\phi$). Such entrapped pixels must be identified and added to the solid fraction ϕ_s . Identifying them requires prior computation of the diffusion in the immobile domain, with the specified boundary conditions, in order to determine the area never visited by the random walkers using the rate-of-visit map (Figure 8). Figure 9

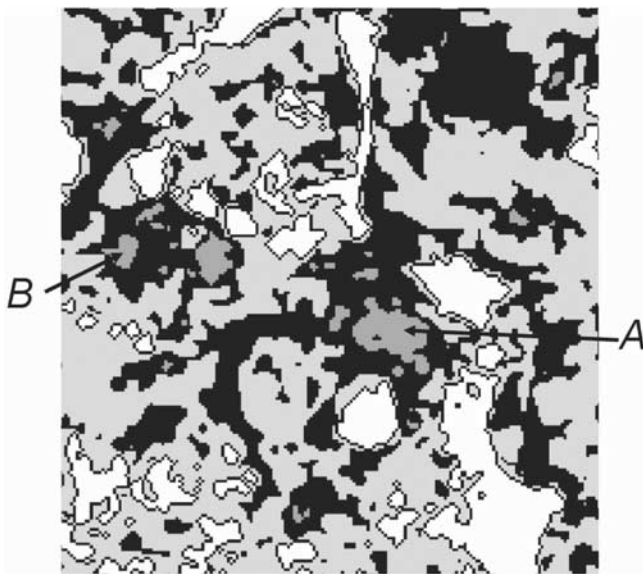


Figure 9. Distribution of ϕ_m and ϕ_s (cross section S1, size 1 mm \times 1 mm) for $\zeta_\phi = 0.6$. White areas represent the mobile domain, and black areas represent the fraction of solid rock where porosity is lower than the threshold value ($\phi'_{im} < \zeta_\phi$). Light gray areas show the fraction of the rock where $\phi'_{im} > \zeta_\phi$ and which is accessible for diffusion. Dark gray areas show the fraction of the rock where $\phi'_{im} > \zeta_\phi$ but which is entrapped within the solid fraction of the rock and therefore is inaccessible for diffusion, for example, the areas indicated by *A* and *B*. The solid fraction, ϕ_s , is composed of the sum of the black and dark gray pixel fractions.

displays, for cross section S1, the mobile domain in white, the fraction of the rock accessible for diffusion in light gray ($\phi'_{im} > \zeta_\phi$), the solid matrix ($\phi'_{im} \leq \zeta_\phi$) in black and the porous matrix ($\phi'_{im} > \zeta_\phi$) entrapped within the solid fraction of the rock and therefore nonaccessible for diffusion in dark gray. Comparing Figure 9 with Figure 8, zones can be distinguished (as indicated by *B*) that are accessible to diffusion if $\zeta_\phi = 0.5$ but surrounded by the solid fraction if ζ_ϕ is set to 0.6. For heterogeneous media, it is expected that the fraction of such inaccessible pixels increases with ζ_ϕ .

4.6. Validation

[58] The algorithm was first validated for the one-dimensional diffusion problem (i.e., slabs and spheres, Figure 2) for which the solution is known [Carrera *et al.*, 1998]. For all these cases, the corresponding slope at early time is the expected value (e.g., -0.5 ± 0.02 for one-dimensional diffusion problems) and relation (6) holds.

[59] In the following, we analyze the sensitivity of three important parameters linked to the numerical solution of the diffusion problem using the XMT images, i.e., the number of random walkers, the length of the walker jump and the effect of the structure pixelization inherent to the XMT imaging procedure.

[60] For any random walk method, a sufficient number of walkers (or particles) are required. Figures 10 and 11 display the computed memory function and the particle rate-of-visit map in the immobile domain respectively, as a function of the number of particles set at the mobile-immobile boundary ($N_{(0)} = 10^4, 10^6$ and 10^9). The rate of

visit is defined as the sum of the particles that have been in a given voxel until all the particles are removed from the immobile domain divided by $N_{(0)}$. Figure 11 shows that a large portion of the immobile domain is not visited if the number of particle $N_{(0)}$ is insufficient. For $N_{(0)}$ less than about 10^9 , the rate-of-visit map changes with $N_{(0)}$ and the diffusion problem is not steady state. For any number of particles, $N_{(0)}$, larger than about 10^9 , the rate-of-visit map is steady state and the diffusion problem can be solved adequately. Nevertheless, the corresponding memory function (Figure 10) shows that most of the characteristics of the memory function are dealt with for $N_{(0)} = 10^6$, emphasizing that the memory function is strongly controlled by the macroscopic (compared to the pixel size) geometry of the mobile-immobile interface, assuming a constant porosity immobile zone.

[61] Acknowledging that the shape of the mobile-immobile interface represents a critical controlling parameter, it is important to evaluate how the pixelization of the media (induced by the XMT imaging process) and the discretization of the diffusion problem (link to the size of the random walker jump) can affect the memory function computation. Figure 12 (left) displays the memory function computed for cross section S4 with a random walk jump ε equal to the size of the pixel, $a = 1$ ($\varepsilon = aL$, with $L = 5.02 \mu\text{m}$), and for $a = 0.1$. Results are practically indistinguishable, indicating that the computation algorithm is independent of the value of ε as long as $\varepsilon \leq L$. Conversely, discretization effects are tested by computing the memory function of simple geometries (slab, sphere or cube) for different scales of pixelization. Figure 12 (right) displays the results obtained for cubes of different sizes (the pixel size is constant) computed before and after a rotation of 45 degrees inducing a pixelization of the structure. The level of pixelization can be measured by the ratio of pixel size to cube size. Results show that pixelization has little effect on the memory function for structures larger than about ten times the pixel size.

5. Results and Discussion

[62] In this section, we compare the memory function computed using the XMT images (microscale approach) to

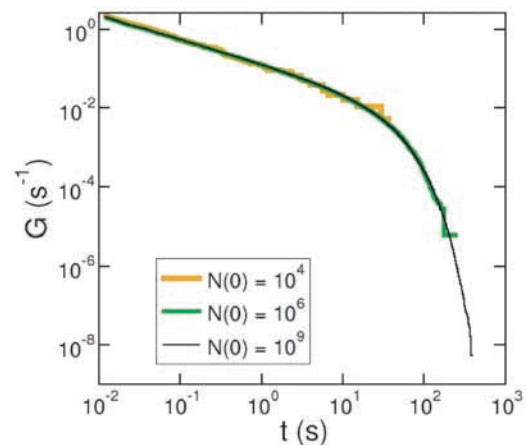


Figure 10. Computed memory function corresponding to the cross sections displayed in Figure 11 for an increasing number of random walkers $N(0)$ ($N(0) = 10^4, 10^6$, and 10^9 , respectively).

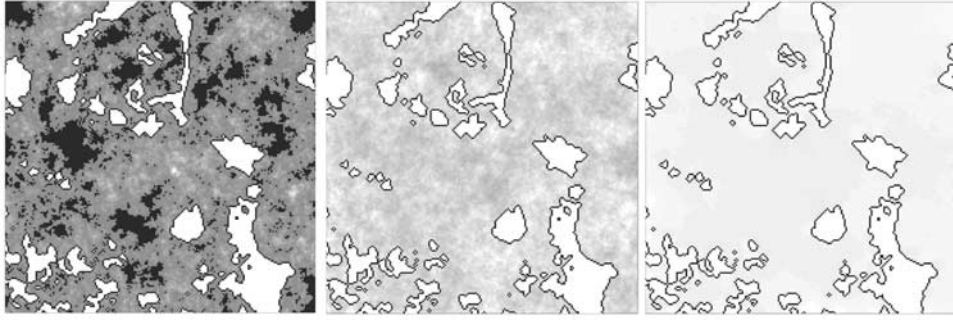


Figure 11. Particle rate-of-visit map (cross section S1) in the immobile domain assuming homogeneous porosity of the immobile zone. White areas bounded by a black line represent the mobile domain. In the immobile domain, dark zones correspond to a low rate of visit, whereas light gray denotes a high rate of visit. From left to right, the number of particles set at the boundary $N(0)$ increases ($N(0) = 10^4$, 10^6 , and 10^9 , respectively). As the number of particles used to compute the memory function increases, both the homogeneity of the visiting of the immobile zone and the statistical representativeness increase (cross section S1; size 1 mm \times 1 mm).

the memory function required to fit the BTCs measured during the SWIW tracer test. As mentioned in section 2, the BTCs (Figure 1) display a power law concentration decrease $C(t) \sim t^{-2}$ at intermediate time $t_{ad} \ll t < t_c$ followed by an asymptotic behavior characterized by $C(t) \sim t^{-1.5}$ for $t > t_c$, with $t_c \approx 2 \times 10^4$ s. Using a CTRW model, *Le Borgne and Gouze* [2008] reproduced these results by implementing a dual slope power law distribution of transition times in the immobile domain, $\psi(t) \sim t^{-\gamma}$ with $\gamma = -2$ for $t < t_c$ and $\gamma = -1.5$ for $t > t_c$ (Figure 1, right). The transition time distribution denotes the retention time probability distribution of the tracer in the immobile domain. *Dentz and Berkowitz* [2003] studied the mathematical equivalence between the transition time distribution used in the CTRW approach to model the mass transfer in the immobile domain and the memory function used in the

MIM mass transfer model. They demonstrated the following equality:

$$\tilde{G}(s) = \frac{1 - \tilde{\psi}(s)(1 + st_1)}{st_1 \tilde{\psi}(s)}, \quad (36)$$

where \tilde{G} and $\tilde{\psi}$ denote the Laplace transform of the memory function and the transition time distribution, respectively. Consequently, for a transition time distribution $\psi(t) \sim t^{-1-\gamma}$ with $\gamma = 1$ for $t < t_c$ and $\gamma = 0.5$ for $t > t_c$, we expect the MIM mass transfer model, described by equations (1)–(5), to be characterized by a dual slope memory function with $G(t) \sim t^{-1}$ for $t < t_c$ and $G(t) \sim t^{-0.5}$ for $t > t_c$. Specifically, assuming a transition time distribution $\psi(t) = C(t/t_1)^{-1-\gamma}$ for $t_{ad} < t < t_c$, the corresponding memory function is $G(t) = C'(t/t_1)^{-\gamma}$ with $C' = C/\gamma$ (a similar equivalence holds for $t > t_c$).

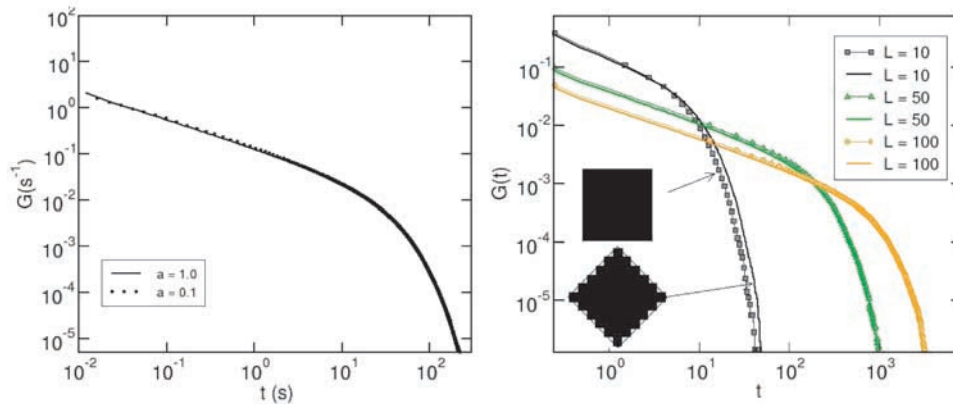


Figure 12. (left) Memory function $G(t)$ computed for cross section S1 for $a = 1$ and 0.1. (right) $G(t)$ computed for square-shaped immobile domains of length $L = 10$, 50, and 100 pixels ($\phi_m = 1$). By rotating the square, the mobile-immobile surface, S_{Ω} , and the mobile-immobile interface roughness are artificially increased. As L increases, the ratio S_{Ω}/V_{im} for the rotated square tends to equal that of the nonrotated square, and the difference between the memory function computed for the rotated and the nonrotated square tends to cancel. However, these results show that the main effect introduced by the artificial increase of S_{Ω}/V_{im} is, as expected, on the memory function breakthrough time and not on the early time slope.

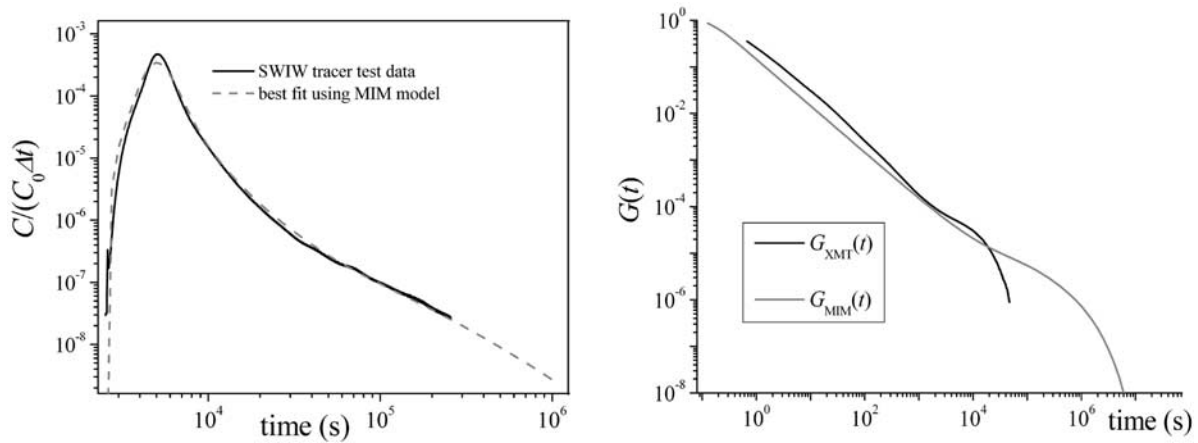


Figure 13. (left) Best fit of the SWIW tracer test BTC for a tracer flush duration of 2400 s using TRANSIN solver. (right) Corresponding memory (G_{MIM}) compared to the memory function G_{XMT} computed using the XMT cross section S4.

In the following, we compute both the pore-scale memory function using XMT cross sections (noted hereafter G_{XMT}) and the reservoir-scale memory function (noted hereafter G_{MIM}) by solving equations (1)–(5) in which the temporal distribution $C(t)$ in the borehole ($x = 0$) is measured during the tracer test. To establish that the microscale diffusion processes in the reservoir matrix control the BTC tailing, the two memory functions G_{MIM} and G_{XMT} must be identical and display the same dual slope behavior as the transition time distribution found by *Le Borgne and Gouze* [2008] (Figure 1).

5.1. Memory Function G_{MIM}

[63] *Le Borgne and Gouze* [2008] modeled the tracer tests with a MIM mass transfer model using a CTRW approach. Here, we use the TRANSIN code, which uses a hybrid method based on the integrodifferential formulation of the problem [Carrera *et al.*, 1998]. This method produces the same results as the random walk method proposed by *Le Borgne and Gouze* [2008], but with the explicit introduction of the memory function. Precisely, equations (1)–(3) for a SWIW configuration are solved using TRANSIN code [Carrera *et al.*, 1998] for a given memory function. Computations are performed in one dimension assuming that the flow field, bounded by the packers, has a cylindrical geometry. The radial coordinate is meshed with 10000 elements of size 4×10^{-4} m.

[64] The G_{MIM} corresponding to the SWIW tracer tests, i.e., the memory function best fits the BTC, is obtained by a trial-and-error method. In TRANSIN, the memory function is fitted by a sum of exponentials, similarly to (13):

$$G(t_D) \equiv \sum_{n=1}^N A_n e^{-B_n t_D}, \quad (37)$$

where $t_D = d_{im} t / L^2$ with L the characteristic length of diffusion and N is found to be optimal for values ≥ 100 . Then, finding the optimal memory function leads to optimization of parameters A_n , B_n , and L . The parameters of the dispersion equation, i.e., ϕ_{im} and ϕ_m , are set using the tomographic data ($\phi_{im}/\phi_m = 2.8$ for $\zeta_\phi = 0.6$) and α (the mobile domain dispersion coefficient) is set to the value

fitted by *Le Borgne and Gouze* [2008] using the CTRW approach ($\alpha = 10^{-3}$ m). The best fit of the BTC using the MIM model and the corresponding memory function, G_{MIM} , are displayed in Figure 13.

[65] The memory function G_{MIM} is characterized by different slopes at early time and late time: $G_{MIM}(t) = C'(t/t_1)^{-\gamma}$ with $\gamma = 1$ for $t < t_c$ and $\gamma = 0.5$ for $t > t_c$. This corresponds to the results obtained for the retention time distribution by *Le Borgne and Gouze* [2008]. The transition time t_c is consistent with that obtained from the CTRW model (2×10^4 s). Note that the memory function shows a cutoff time of approximately 10^6 s. However, no cutoff time can be identified from the tracer tests. If it exists, it is larger than the tracer test duration. Thus, we do not have experimental constraints on this cutoff time, except that it should be larger than the maximum elapsed time of the tracer test ($\approx 2 \times 10^5$ s).

5.2. Memory Function G_{XMT}

[66] The algorithm described in section 4 is applied to the Mallorca limestone samples (cross section S4). All the parameters of the problem are known (see Figure 6) except for two: the tortuosity of the diffusion path in the immobile domain and the value of the porosity at the percolation threshold, ζ_ϕ , below which diffusion paths are not connected (see Figure 3c). Results for different values of ζ_ϕ ranging from 0 to 0.6, are reported in Figure 14 together with the memory function obtained assuming that the immobile domain has a constant porosity equal to its arithmetic mean $\langle \phi'_{im} \rangle$, for comparison.

[67] The tortuosity of the diffusion path is certainly the most important parameter controlling the effective diffusion of the tracers, together with the mobile-immobile interface geometry. The latter is measured, with a given resolution, by XMT and will be considered here as known. Conversely, tortuosity is a lumped parameter quantifying the weakening effect of the sinuosity and the interconnectedness of the pore space on diffusion transport. Tortuosity for diffusion transport in heterogeneous porous media cannot be measured without solving the diffusion problem itself, which would require a much better spatial resolution to tackle the microporosity geometry. Often, tortuosity is simply identi-

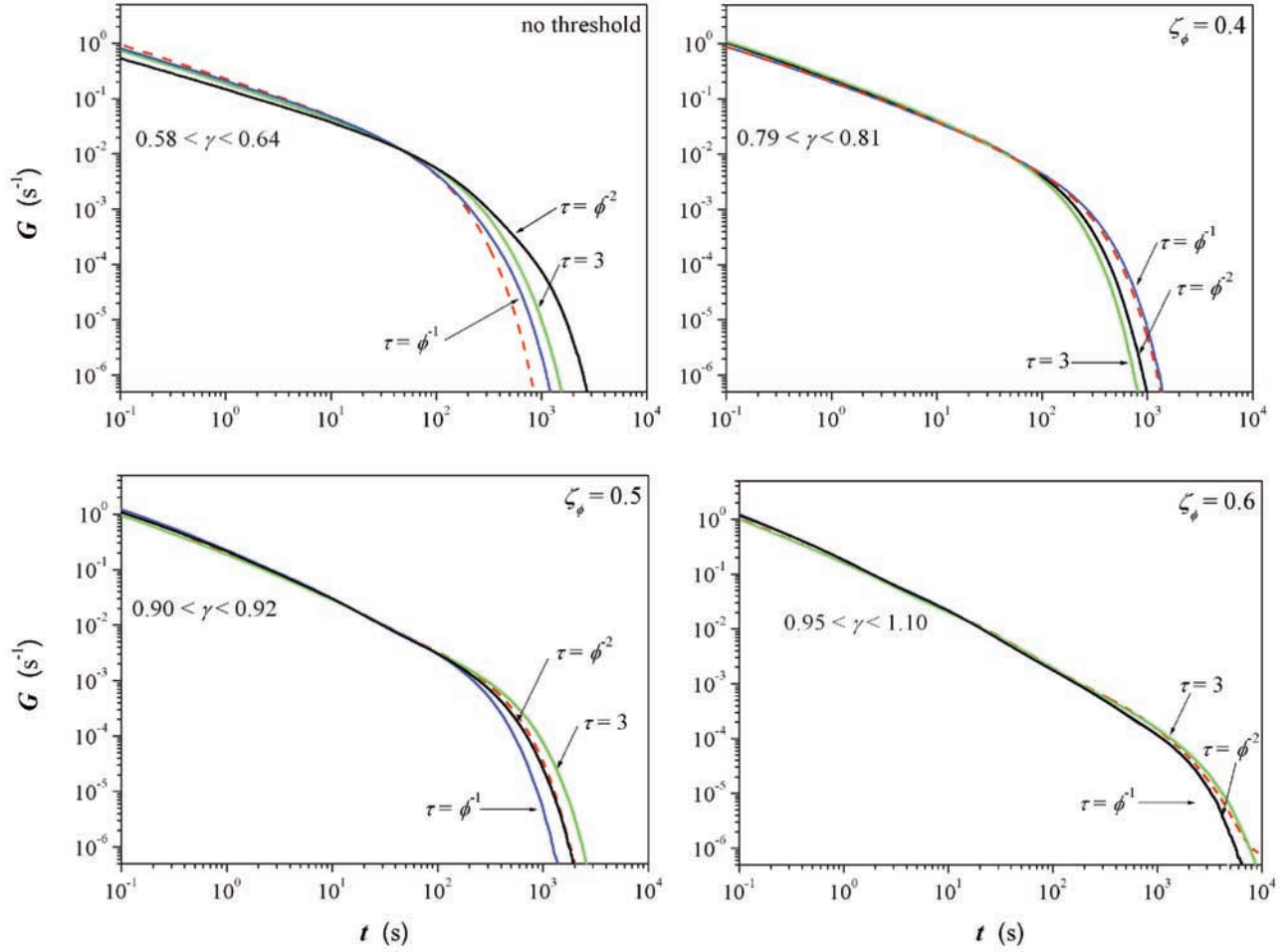


Figure 14. Memory function computed for cross section S1. Solid curves are for heterogeneous porosity with variable tortuosity $\tau(\mathbf{x}') = (\phi'_{im}(\mathbf{x}'))^{-n}$ and constant tortuosity $\tau = 3$. Dashed curves are for constant porosity and tortuosity ($\phi'_{im} = \langle \phi'_{im}(\mathbf{x}') \rangle / \tau$, with $\tau = 3$).

fied with the standard electrical tortuosity (i.e., tortuosity deduced from electrical conductivity measurements) which measures the tortuosity of the pore space affecting the mobility of electrons in a force field. As already discussed in section 4.3, a power law relationship, $\tau \sim \phi^{-n}$, is usually found when measuring electrical tortuosity and we will assume that it is a pertinent approximation. Then, the effective diffusion at location \mathbf{x} in the immobile domain is simply given by $d_{im}(\mathbf{x}) = d_0(\phi'_{im}(\mathbf{x}))^{1+n}$, as already mentioned in section 4.3 (equation (17)).

[68] We plotted (Figure 14) the computed memory functions for $d_{im}(\mathbf{x}) = \phi'_{im}(\mathbf{x})^{n+1}$ with $1 \leq n \leq 2$. For comparison, we also plotted, in the Figure 14, the memory functions computed with a constant tortuosity ($\tau_{im} = 3$) by equations $d_{im}(\mathbf{x}) = \phi'_{im}(\mathbf{x})/\tau_{im}$ and $d_{im}(\mathbf{x}) = \langle \phi'_{im} \rangle / \tau_{im}$ corresponding to cases for which the porosity distribution is taken into account or not respectively. The influence of the tortuosity value on the memory function shape is weak for $n \leq 2$. Conversely, the value of the porosity at the percolation threshold controls the slope of the memory function. For $\zeta_\phi = 0.6$, which is a realistic value according to percolation theory (see section 4.2.4), the slope of the memory function is very close to the value measured on the tracer test BTCs $C(t) \sim t^{-1-\gamma} \approx t^{-2}$ at intermediate time $t_{ad} < t < t_c$.

[69] The memory function has been computed for cross section S1 and three subareas (S2, S3, and S4, see Figure 4). Results are compared in Figure 15 in order to evaluate the representativeness of the computations depending on the choice and the size of the sampled domain. Results show that the memory function slopes are similar, although moderate differences on the late-time breakthrough, i.e., the cutoff time t_{res} , are observed. However, we are mainly interested in the memory function slope, because BTCs are not measured up to t_{res} .

[70] We concentrate now on the asymptotic behavior, $C(t) \sim t^{-1.5}$ for $t_c < t < t_{res}$ that is measured by the SWIW tracer tests. To model this behavior, we assume that larger values of n can be used as an heuristic model to account for larger tortuosity of the microporous matrix using the relation $\tau \sim \phi^{-n}$. Figure 16 summarizes the results obtained for $1 < n < 5$ with $\zeta_\phi = 0.6$. For $n = 5$ (i.e., $d_{im} \sim \phi^6$), the dual slope memory function with an asymptotic slope $C(t) \sim t^{-1.5}$ is obtained. To our knowledge, such high values of n have not been reported in the literature yet. Standard models fitted to tortuosity measurement using electrical potential techniques show values ranging from 2.5 to 4 [Avellaneda and Torquato, 1991; Adler and Thovert, 1998; Boving and Grathwohl, 2001]. Nevertheless, six points must

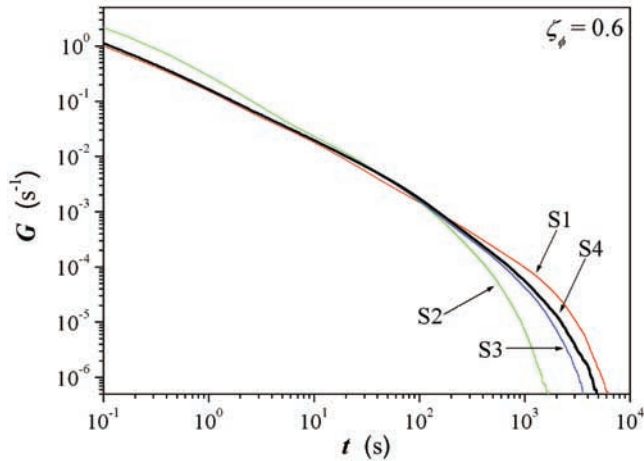


Figure 15. Memory function computed for subdomains S1, S2, S3 (200×200 pixels), and S4 (510×510 pixels), located as indicated in Figure 4.

be considered in order to understand the origin of this apparent uncommon value. First, tortuosity deduced from standard measurements denotes the tortuosity of the percolating cluster (e.g., the porosity cluster connected to the electrodes), while here long-lasting diffusion is expected in dead-end structures. Second, such measurements on cores quantify the tortuosity of the bulk rock, i.e., immobile and mobile domains. Third, the electrical tortuosity can be expected to be different from the tortuosity affecting diffusion in the immobile domain [Ben Clennell, 1997]. Fourth, we do not explicitly take into account the constrictivity effect which is expected to be correlated with the porosity. In our model, constrictivity can be considered to be integrated in the tortuosity model, hence increasing the dependence of τ with ϕ . Fifth, it is expected that n is large close to the percolation threshold, by analogy with the permeability-porosity relationship [Martys et al., 1994]; the average porosity of the diffusion paths is probably close to the value of the porosity at the percolation threshold in the deep matrix. Finally, high value of n may be considered as a proxy to account for the fractal nature of the pore space that is superimposed on the porosity heterogeneity and the block matrix shape nonuniformity [Liu et al., 2007]; however, at this point, we do not have the means to measure the fractal properties of the matrix at small scales (i.e., $< \mu\text{m}$).

5.3. Comparison of G_{XMT} Versus G_{MIM}

[71] The memory function G_{XMT} obtained for $\zeta_\phi = 0.6$ and $n = 5$ and the memory function G_{MIM} fitted from the SWIW tracer tests are compared in Figure 13. The two memory functions are similar at first ($t < 10^3$), which emphasizes that the scaling of the memory function G_{MIM} for the shortest diffusion times is well explained by pore-scale diffusion processes. However, the value of the transition time between $G(t) \sim t^{-1}$ behavior and $G(t) \sim t^{-0.5}$ behavior is noticeably smaller (almost one decade) for the pore-scale computed memory function G_{XMT} . Similarly, the cutoff time is about two decades less than the minimum cutoff time required to fit the tracer test data (Figure 13).

[72] Apparently, the residence time of the tracer in the immobile domain is underestimated when computed using

the XMT cross sections. The main explanation is probably linked to the fact that calculations were carried out on cross sections (2-D); longer diffusion paths than those observed in two dimensions are expected in three dimensions and the effective value of the porosity at the percolation threshold should be different. Considering that the dual slope behavior is controlled by both the matrix block shape and the heterogeneity of the porosity, 3-D computations will probably stretch the time axis if diffusion paths are longer. Computations presented in this paper can be implemented in three dimensions without any algorithmic difficulties, but this will require large computational resources in order to maintain a sufficiently large domain in the three directions. This computation should be tractable in the near future.

[73] The underestimation of the trapping time of the tracer in the immobile domain may also be due to the poorly constrained relationship we use to relate the local porosity and the local diffusion coefficient. Figure 16 shows that the transition from $G(t) \sim t^{-1}$ to $G(t) \sim t^{-0.5}$ is strongly sensitive to the spatial distribution of d_{im} . For instance, the tortuosity of the diffusion paths, as well as the variability and the spatial correlation of the diffusivity along the paths are probably imperfectly modeled by a relation of the form $d_{im} \sim \phi^n$. The XMT data presented in this paper cannot produce much more information on the dispersivity distribution. However, preliminary results [see Gouze et al., 2008, Figure 6] show that using better resolution XMT images, i.e., voxel sizes smaller than $1 \mu\text{m}$, it is possible to accurately distinguish the solid fraction from the voids. In this case, the structure of the microporosity should be better modeled and small-scale computation of diffusion in the immobile inframetric matrix clusters may be possible. This will be the object of a future publication.

[74] Another source of uncertainty in the characteristics of the immobile domain is the approximation made when determining the sample-spanning cluster from which we compute the mobile domain and the dead-end structures. The diffusive fraction of the sample-spanning cluster was obtained through a technique that minimizes its volume. Indeed, we determine the dead ends from the union of the advection backbone computed assuming flow in each of the principal directions (Figure 5). We may expect that for

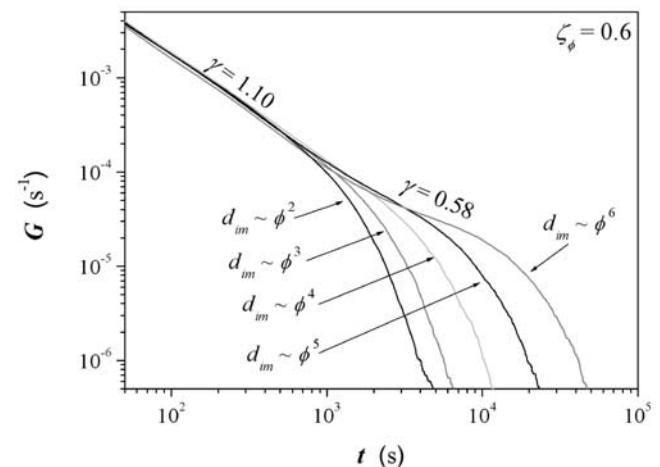


Figure 16. Memory function computed for increasing values of n ($1 < n < 5$) with $d_{im} \sim (\phi'_{im})^{n+1}$.

directional flow, such as imposed by the boundary conditions at the well, larger no-flow zones may exist. However, note that the uncertainties linked to the determination of the mobile domain and of the macropore dead-end properties are not expected to control the memory function for large time because the diffusion in immobile water zones is much faster than in the microporous matrix.

[75] Moreover, size effect can be viewed as well as a potential source of uncertainty. Specifically, the sample-spanning cluster (from which ϕ_m is resolved) is determined from a small-scale volume of rock (about 3 mm³). It is possible that this sample-spanning cluster was not representative of the cluster in relation to the tracer injection zone. For instance, larger volumes of rock unconnected with the main large-scale cluster may exist. However, the probability of occurrence of such zones is certainly low because of the large porosity of the reservoir, and it can be anticipated that the memory function will not be significantly altered.

6. Conclusions

[76] In their mobile-immobile mass transfer model, *Carrera et al.* [1998] and *Haggerty et al.* [2000] proposed to link the non-Fickian dispersion observed on tracer test BTCs at laboratory scale to field scale, to microscale diffusion processes within water immobile zones. The assumption made in this model has strong implications on the way we can predict dispersion in porous reservoirs, because it implicitly states that large-scale non-Fickian dispersion is controlled by the microscale (possibly spatially distributed) properties of the media.

[77] MIM mass transfer models have been applied successfully to interpret BTCs by fitting theoretical memory functions (or transition time distributions in the case of the CTRW formulation). Nevertheless, these memory functions have never been directly measured in the case of in situ tracer tests, and it can be questioned whether the memory function, implemented in the sink/source term of the transport equation, is just a practical way to increase the degree of liberty for fitting the tracer test BTCs, or models precisely the physics of the tracer transport. This questioning is reinforced by the fact that other processes, for instance linked to spatial correlations of the velocity field, have been proposed to explain heavy tailed non-Fickian BTCs [e.g., *Benson et al.*, 2001; *Berkowitz and Scher*, 1998]. Direct experimental confirmation of velocity distribution-controlled non-Fickian dispersion is lacking, but there is evidence that, in certain cases, matrix diffusion is unlikely to be at the origin of the non-Fickian dispersion behavior. For instance, *Becker and Shapiro* [2000] conducted tracer tests in a fractured aquifer using three tracers displaying different diffusion coefficients. They measured similar BTCs with power tailing $C(t) \sim t^{-2}$ for all the tracers, whereas matrix diffusion should have produced dissimilar BTCs according to the dissimilar diffusivity of the tracers. Later, the authors fitted nicely the tracer test BTCs with a model in which channelized transport is conceptually controlled by parallel fractures with distributed apertures [*Becker and Shapiro*, 2003]. The relation between the velocity distribution (and its correlation structure) and the properties of the permeability distribution for realistic geological media is a debated issue [e.g., *Le Borgne et al.*,

2007], however, it is expected that long-range velocity correlations should result from long-range connectivity structures. For the high-porosity reservoir investigated in this paper, no long-range connectivity structure is observed at the scale of the tracer tests (i.e., meter scale [*Gouze et al.*, 2008]). Hence, in this nonfractured porous media, diffusion-like advective processes such as proposed by *Becker and Shapiro* [2000, 2003] are unlikely to produce long-lasting BTC tail with $C(t) \sim t^{-1.5}$.

[78] In this paper we first presented a technique to measure the memory function from reservoir samples and then we compared the result with the memory function fitted from a set of SWIW tracer tests performed in the same reservoir. We detail step by step the method for computing the memory function using micrometer-scale description of the matrix structure and properties measured by the way of X-ray microtomography. The memory function is mainly controlled by the geometry of the mobile-immobile interface, the distribution of the immobile zones and the tortuosity of the diffusion paths within each of the immobile zones. The XMT technique and the original data processing presented in this paper appears to be well adapted to determine the geometry of the immobile domain and its interface with the mobile domain, as well as the porosity of the immobile domain. We observed that the $\log(G) - \log(t)$ slope of the memory function is very sensitive to the value of the porosity at the percolation threshold ζ_ϕ . This was expected because ζ_ϕ determines both the geometry of the mobile-immobile interface and the shape of the immobile clusters, and therefore determines the residence time distribution in the immobile domain. The scaling $G(t) \sim t^{-1.0}$ measured during the field-scale tracer tests is reproduced for a value of $\zeta_\phi \approx 0.6$.

[79] Conversely, the tortuosity that specifies the intrinsic geometry of the diffusion path cannot be achieved deterministically with an XMT resolution of 5.02 μm . A classical empirical relationship, $\tau_{im} \sim \phi_{im}^{-n}$, was used to determine the percolation paths and their tortuosity from the porosity. This relation was used as a proxy to evaluate the tortuosity (and implicitly the constrictivity) assuming that it depended on the porosity only. At this point, the value of n was not constrained by any external measurement, and a sensitivity analysis of the value of n was therefore performed. We observed that increasing the value of n modified the late-time slope of the memory function without influencing the first part of the BTC tail. A dual slope memory function was obtained for $n > 4$. A $\log(G) - \log(t)$ slope of -0.5 was obtained for $n = 5$. It represents the occurrence of large residence time zones in the immobile domain. Within the framework of classical models, $G(t) \sim t^{-0.5}$ is attributed to infinitely large matrix blocks or a uniform distribution of block size.

[80] At this point, we have replaced the two probably distribution parameters that characterize the transition time distribution (Figure 1) with two semiempirical physical parameters. The value of the first one, the porosity at the percolation threshold ζ_ϕ , corresponds unsurprisingly to the average value of 0.6 obtained for most of the 2-D pore shape models. Conversely, the second one, the tortuosity, cannot be related to previously measured values because the tortuosity of intergrain diffusion dead-end structures cannot be measured directly by conventional potentiometric

techniques (i.e., electrical measurements). We found that reproducing the asymptotic behavior $G(t) \sim t^{-0.5}$ measured during the tracer tests requires that the 2-D tortuosity of the diffusion path in the matrix is in average larger than 5; that is, that the length of the effective diffusion paths lengths are in average larger than 5 times their topologic length. We have no means to extrapolate this value in three dimensions, but it is probable, that bulk matrix tortuosity is lower than the tortuosity of its projection in two dimensions, and should approach standard values (i.e., $2.5 < n < 4$).

[81] Following the empirical relation $\tau_{im} \sim \phi_{im}^{-n}$ with $\phi_{im} \geq 0.6$ and $n = 5$, the memory function computed from XMT images, $G_{XMT}(t)$, is similar to the memory function, $G_{MIM}(t)$, deduced from the field-scale tracer tests. Both the dual slope behavior and the values of the two slopes are similar. However, the overall matrix diffusivity appears to be underestimated. We attribute this to the use of 2-D measurements and to cumulative inaccuracies in the evaluation of the effective tortuosity. These inaccuracies may originate from both the resolution cutoff related to the XMT method and the assumption that tortuosity (and constrictivity) depends on porosity only. The occurrence of non-Fickian dispersion, linked to the possible fractal nature of the diffusion path at submicrometer scales, is also a possible source of matrix diffusivity underestimation. Nevertheless, results show that the atypical non-Fickian dispersion measured from the tracer tests at the Ses Sitjoles test site is well explained by microscale diffusion processes in the matrix. The MIM model therefore appears to be valid for this specific case.

[82] This study emphasizes that measuring the matrix residence time of rocks is essential for the validation of dispersion models and for the development of relevant pollution risk assessment tools. Without a doubt, the major challenge lies in measuring the matrix porosity and the parameters that limit diffusion (e.g., tortuosity), and in localizing zones where fluid can be considered to be immobile. The XMT technique appears to be a promising tool to capture the properties of the immobile domain and allows computing the memory function. The results presented here show that the main characteristics of matrix diffusion are captured by 2-D calculations. Nevertheless, the procedure must be improved to better constrain the memory function for longer residence times. Three-dimensional computations and the assessment of matrix structure with a better XMT resolution should provide a more accurate definition of the memory function.

[83] **Acknowledgments.** The authors wish to acknowledge the support of the European project Advanced Logging Investigations In Coastal Environments (ALIANCE), contract EKV-2001-00039. M.D. acknowledges the support of the Spanish Ministry of Education and Science (MEC) through the program Ramón y Cajal and the project MODEST (CGL-2005-05171). We thank Matthew Becker, Sean McKenna, and an anonymous reviewer for their valuable comments that have helped to improve the original manuscript.

References

- Adams, E. E., and L. W. Gelhar (1992), Field study of dispersion in a heterogeneous aquifer: 2. Spatial moment analysis, *Water Resour. Res.*, *28*(12), 3293–3308, doi:10.1029/92WR01757.
- Adler, P. M., and J. F. Thovert (1998), Real porous media: Local geometry and macroscopic properties, *Appl. Mech. Rev.*, *51*(9), 537–585.
- Avellaneda, M., and S. Torquato (1991), Rigorous link between fluid permeability, electrical conductivity, and relaxation times for transport in porous media, *Phys. Fluids A*, *3*(11), 2529–2540, doi:10.1063/1.858194.
- Baker, D. R., G. Paul, S. Sreenivasan, and H. E. Stanley (2002), Continuum percolation threshold for interpenetrating squares and cubes, *Phys. Rev. E*, *66*, 046136, doi:10.1103/PhysRevE.66.046136.
- Balberg, I. (1985), Universal percolation-threshold limits in the continuum, *Phys. Rev. B*, *31*(6), 4053–4055, doi:10.1103/PhysRevB.31.4053.
- Becker, M. W., and A. M. Shapiro (2000), Tracer transport in fractured crystalline rock: Evidence of nondiffusive breakthrough tailing, *Water Resour. Res.*, *36*(7), 1677–1686, doi:10.1029/2000WR900080.
- Becker, M. W., and A. M. Shapiro (2003), Interpreting tracer breakthrough tailing from different forced-gradient tracer experiment configurations in fractured bedrock, *Water Resour. Res.*, *39*(1), 1024, doi:10.1029/2001WR001190.
- Ben Clennell, M. (1997), Tortuosity: A guide through the maze, *Geol. Soc. Spec. Publ.*, *122*, 299–344.
- Benson, D. A., R. Schumer, M. M. Meerschaert, and S. W. Wheatcraft (2001), Fractional dispersion, Lévy motion, and the MADE tracer tests, *Transp. Porous Media*, *42*, 211–240, doi:10.1023/A:1006733002131.
- Berkowitz, B., and H. Scher (1998), Theory of anomalous chemical transport in random fracture networks, *Phys. Rev. E*, *57*(5), 5858–5869.
- Berkowitz, B., H. Scher, and S. E. Silliman (2000), Anomalous transport in laboratory-scale, heterogeneous porous media, *Water Resour. Res.*, *36*(1), 149–158, doi:10.1029/1999WR900295.
- Berkowitz, B., J. Klafter, R. Metzler, and H. Scher (2002), Physical pictures of transport in heterogeneous media: Advection-dispersion, random-walk and fractional derivative formulations, *Water Resour. Res.*, *38*(10), 1191, doi:10.1029/2001WR001030.
- Bernard, D., Ø. Nielsen, L. Salvo, and P. Cloetens (2005), Permeability assessment by 3D interdendritic flow simulations on microtomography mappings of Al-Cu alloys, *Mater. Sci. Eng. A*, *392*(1–2), 112–120, doi:10.1016/j.msea.2004.09.004.
- Boving, T. B., and P. Grathwohl (2001), Tracer diffusion coefficients in sedimentary rocks, Correlation to porosity and hydraulic conductivity, *J. Contam. Hydrol.*, *53*(1–2), 85–100, doi:10.1016/S0169-7722(01)00138-3.
- Carrera, J., J. Samper, G. Galarza, and A. Medina (1990), An approach to process identification: Application to solute transport through clays, ModelCARE90, in *Calibration and Reliability in Groundwater Modeling*, edited by K. Kovar, *IAHS Publ.*, *195*, 231–240.
- Carrera, J., X. Sánchez-Vila, I. Benet, A. Medina, G. Galarza, and J. Guimerà (1998), On matrix diffusion, Formulations, solutions methods and qualitative effects, *Hydrogeol. J.*, *6*(1), 178–190, doi:10.1007/s100400050143.
- Coats, K. H., and B. D. Smith (1964), Dead-end pore volume and dispersion in porous media, *J. Soc. Pet. Eng.*, *4*, 73–84.
- de Marsily, G. (1986), *Quantitative Hydrogeology*, Academic, San Diego, Calif.
- Dentz, M., and B. Berkowitz (2003), Transport behavior of a passive solute in continuous time random walks and multirate mass transfer, *Water Resour. Res.*, *39*(5), 1111, doi:10.1029/2001WR001163.
- Dentz, M., A. Cortis, H. Scher, and B. Berkowitz (2004), Time behavior of solute transport in heterogeneous media: Transition from anomalous to normal transport, *Adv. Water Resour.*, *27*, 155–173, doi:10.1016/j.advwatres.2003.11.002.
- Dias, R., J. A. Teixeira, M. Mota, and A. Yelshin (2006), Tortuosity variation in a low density binary particulate bed, *Sep. Purif. Technol.*, *51*, 180–184, doi:10.1016/j.seppur.2006.01.010.
- Dullien, F. A. L. (1992), *Porous Media Fluid Transport and Pore Structure*, 574 pp., Academic, San Diego, Calif.
- Garboczi, E. J., K. A. Snyder, J. F. Douglas, and M. F. Thorpe (1995), Geometrical percolation threshold of overlapping ellipsoids, *Phys. Rev. E*, *52*(1), 819–828, doi:10.1103/PhysRevE.52.819.
- Gelhar, L. W., and M. A. Collins (1971), General analysis of longitudinal dispersion in nonuniform flow, *Water Resour. Res.*, *7*(6), 1511–1521, doi:10.1029/WR007i006p01511.
- Gouze, P., T. Le Borgne, R. Leprovost, G. Lods, T. Poidras, and P. Pezard (2008), Non-Fickian dispersion in porous media: 1. Multiscale measurements using single-well injection withdrawal tracer tests, *Water Resour. Res.*, *44*, W06426, doi:10.1029/2007WR006278.
- Guimerà, J., and J. Carrera (2000), A comparison of hydraulic and transport parameters measured in low permeability fractured media, *J. Contam. Hydrol.*, *41*, 261–281, doi:10.1016/S0169-7722(99)00080-7.
- Haggerty, R., and S. M. Gorelick (1995), Multiple-rate mass transfer for modeling diffusion and surface reactions in media with pore-scale heterogeneity, *Water Resour. Res.*, *31*(10), 2383–2400.

- Haggerty, R., S. A. McKenna, and L. C. Meigs (2000), On the late-time behavior of tracer test breakthrough curves, *Water Resour. Res.*, 36(12), 3467–3480, doi:10.1029/2000WR900214.
- Haggerty, R., S. W. Fleming, L. C. Meigs, and S. A. McKenna (2001), Tracer tests in a fractured dolomite: 2. Analysis of mass transfer in single-well injection-withdrawal tests, *Water Resour. Res.*, 37(5), 1129–1142, doi:10.1029/2000WR900334.
- Haggerty, R., C. F. Harvey, C. Freiherr von Schwerin, and L. C. Meigs (2004), What controls the apparent timescale of solute mass transfer in aquifers and soils? A comparison of experimental results, *Water Resour. Res.*, 40, W01510, doi:10.1029/2002WR001716.
- Heer, W., and J. Haderman (1994), Modelling radionuclide migration—Field experiments, *Ber. 94-13*, Paul Scherrer Inst., Villigen, Switzerland.
- Hunt, A. (2005), Continuum percolation theory for transport properties in porous media, *Philos. Mag.*, 85(29), 3409–3434, doi:10.1080/14786430500157094.
- Khrapitchev, A. A., and P. T. Callaghan (2003), Reversible and irreversible dispersion in a porous medium, *Phys. Fluids*, 15, 2649–2660, doi:10.1063/1.1596914.
- Le Borgne, T., and P. Gouze (2008), Non-Fickian dispersion in porous media: 2. Model validation from measurements at different scales, *Water Resour. Res.*, 44, W06427, doi:10.1029/2007WR006279.
- Le Borgne, T., J.-R. de Dreuzy, P. Davy, and O. Bour (2007), Characterization of the velocity field organization in heterogeneous media by conditional correlation, *Water Resour. Res.*, 43, W02419, doi:10.1029/2006WR004875.
- Levy, M., and B. Berkowitz (2003), Measurement and analysis of non-Fickian dispersion in heterogeneous porous media, *J. Contam. Hydrol.*, 64(3–4), 203–226, doi:10.1016/S0169-7722(02)00204-8.
- Liu, H. H., Y. Q. Zhang, Q. Zhou, and F. J. Molz (2007), An interpretation of potential scale dependence of the effective matrix diffusion coefficient, *J. Contam. Hydrol.*, 90(1–2), 41–57, doi:10.1016/j.jconhyd.2006.09.006.
- Martys, N. S., S. Torquato, and D. P. Bentz (1994), Universal scaling of fluid permeability for sphere packings, *Phys. Rev. E*, 50(1), 403–408, doi:10.1103/PhysRevE.50.403.
- Meigs, L. C., and R. L. Beauheim (2001), Tracer tests in a fractured dolomite, 1, Experimental design and observed tracer recoveries, *Water Resour. Res.*, 37(5), 1113–1128, doi:10.1029/2000WR900335.
- Neher, R. A., K. Mecke, and H. Wagner (2008), Topological estimation of percolation thresholds, *J. Stat. Mech.*, P01011, doi:10.1088/1742-5468/2008/01/P01011.
- Neretnieks, I. (1980), Diffusion in the rock matrix: An important factor in radionuclide retardation?, *J. Geophys. Res.*, 85(B8), 4379–4397, doi:10.1029/JB085iB08p04379.
- Noiriel, C., B. Madé, and P. Gouze (2007), Impact of coating development on the hydraulic and transport properties in argillaceous limestone fracture, *Water Resour. Res.*, 43, W09406, doi:10.1029/2006WR005379.
- Risken, H. (1996), *The Fokker-Planck Equation*, Springer, New York.
- Sardini, P., F. Delay, K.-H. Hellmuth, G. Porel, and E. Oila (2003), Interpretation of out-diffusion experiments on crystalline rocks using random walk modeling, *J. Contam. Hydrol.*, 61(1–4), 339–350, doi:10.1016/S0169-7722(02)00124-9.
- Sardini, P., J. C. Robinet, M. Siitari-Kauppi, F. Delay, and K. H. Hellmuth (2007), Direct simulation of heterogeneous diffusion and inversion procedure applied to an out-diffusion experiment. Test case of Palmottu granite, *J. Contam. Hydrol.*, 93(1–4), 21–37, doi:10.1016/j.jconhyd.2007.01.011.
- Schumer, R., D. A. Benson, M. M. Meerschaert, and B. Baeumer (2003), Fractal mobile/immobile solute transport, *Water Resour. Res.*, 39(10), 1296, doi:10.1029/2003WR002141.
- Shapiro, A. M. (2001), Effective matrix diffusion in kilometer-scale transport in fractured crystalline rock, *Water Resour. Res.*, 37(3), 507–522, doi:10.1029/2000WR900301.
- Silliman, S. E., and E. S. Simpson (1987), Laboratory evidence of the scale effect in dispersion of solutes in porous media, *Water Resour. Res.*, 23(8), 1667–1673, doi:10.1029/WR023i008p01667.
- Stanley, D. R. (1983), *The Radon Transform and Some of its Applications*, John Wiley, New York.
- Stauffer, D., and A. Aharony (1994), *Introduction to Percolation Theory*, Taylor and Francis, London.
- Torquato, S. (2001), *Random Heterogeneous Materials*, Springer, New York.
- Tsang, Y. W. (1995), Study of alternative tracer tests in characterizing transport in fractured rocks, *Geophys. Res. Lett.*, 22(11), 1421–1424, doi:10.1029/95GL01093.
- van Genuchten, M. T., and P. J. Wierenga (1976), Mass transfer studies in sorbing porous media I. Analytical solutions, *Soil Sci. Soc. Am. J.*, 40, 473–480.
- Wood, W. W., T. F. Kraemer, and P. P. Hearn Jr. (1990), Intragranular diffusion: An important mechanism influencing solute transport in clastic aquifers?, *Science*, 247, 1569–1572, doi:10.1126/science.247.4950.1569.
- Zhou, Q., H.-H. Liu, F. J. Molz, Y. Zhang, and G. S. Bodvarsson (2007), Field-scale effective matrix diffusion coefficient for fractured rock: Results from literature survey, *J. Contam. Hydrol.*, 93, 161–187, doi:10.1016/j.jconhyd.2007.02.002.

J. Carrera, Institute of Earth Sciences Jaume Almera, CSIC, C/Lluís Sole Sabaris s/n, E-08028 Barcelona, Spain.

M. Dentz, Department of Geotechnical Engineering and Geosciences, Technical University of Catalonia, C/Jordi Girona, 1-3, E-08034 Barcelona, Spain.

P. Gouze, T. Le Borgne, and Y. Melean, Géosciences, Université de Montpellier 2, CNRS, F-34095 Montpellier CEDEX 5, France. (philippe@msem.univ-montp2.fr)